Published in final edited form as:

Nat Cancer. 2022 August ; 3(8): 976–993. doi:10.1038/s43018-022-00405-x.

Transition to a mesenchymal state in neuroblastoma confers resistance to anti-GD2 antibody via reduced expression of ST8SIA1

Nathaniel W. Mabe[1,2,17], **Min Huang**[3,17], **Guillermo N. Dalton**[3], **Gabriela Alexe**[1,2], **Daniel A. Schaefer**[1], **Anna C. Geraghty**[4], **Amanda L. Robichaud**[1], **Amy S. Conway**[1], **Delan Khalid**[1], **Marius M. Mader**[5,6], **Julia A. Belk**[7], **Kenneth N. Ross**[1,2], **Michal Sheffer**[8], **Miles H. Linde**[9,10], **Nghi Ly**[6], **Winnie Yao**[6], **Maria Caterina Rotiroti**[3], **Benjamin A. H. Smith**[11], **Marius Wernig**[5,6], **Carolyn R. Bertozzi**[12,13], **Michelle Monje**[4,13], **Constantine S. Mitsiades**[8], **Ravindra Majeti**[9], **Ansuman T. Satpathy**[6,14], **Kimberly Stegmaier**[1,2,18], **Robbie G. Majzner**[3,15,16,18]

[1]Department of Pediatric Oncology, Dana-Farber Cancer Institute and Boston Children's Hospital, Boston, MA, USA.

[2]Broad Institute of MIT and Harvard, Cambridge, MA, USA.

[3]Department of Pediatrics, Stanford University School of Medicine, Stanford, CA, USA.

[4]Department of Neurology and Neurological Sciences, Stanford University, Stanford, CA, USA.

[5]Institute for Stem Cell Biology and Regenerative Medicine, Stanford, CA, USA.

[6]Department of Pathology, Stanford University School of Medicine, Stanford, CA, USA.

[7]Department of Computer Science, Stanford University School of Medicine, Stanford, CA, USA.

[8]Department of Medical Oncology, Dana-Farber Cancer Institute, Boston, MA, USA.

Kimberly_stegmaier@dfci.harvard.edu; rmajzner@stanford.edu.

Author contributions

N.W.M., M.H., K.S. and R.G.M. conceived of the project. N.W.M., M.H., N.D., D.A.S., A.C.G., M.M.M., M.L., N.L., W.Y., M.C.R., B.A.H.S., C.M., R.M., A.S., K.S. and R.G.M. generated data. M.S. and C.M. provided NK cell cultures and guidance. N.W.M., M.H., N.D., H.A., A.C.G., M.M.M., J.A.B., B.A.H.S., K.S. and R.G.M. analyzed data. N.W.M., M.H., N.D., A.S.C., M.M.M., M.L., B.A.H.S., M.C.R., M.W., C.R.B., M.M., C.M., R.M., A.T.S., K.S. and R.G.M. helped design experiments. N.D., A.L.R., A.S.C. an D.K. planned and executed in vivo studies. N.W.M., G.A., J.A.B., K.N.R. and A.T.S. provided bioinformatics analysis. N.W.M., K.S. and R.G.M. wrote the manuscript. All authors reviewed the manuscript.

Competing interests

The remaining authors declare no competing interests.

Additional information

Extended data is available for this paper at https://doi.org/10.1038/s43018-022-00405-x.

Supplementary information The online version contains supplementary material available at https://doi.org/10.1038/s43018-022-00405-x.

Correspondence and requests for materials should be addressed to Kimberly Stegmaier or Robbie G. Majzner.

Peer review information *Nature Cancer* thanks Christian Capitini and the other, anonymous, reviewer(s) for their contribution to the peer review of this work.

Reprints and permissions information is available at www.nature.com/reprints.

[9]Department of Medicine, Division of Hematology, Stanford University School of Medicine, Stanford, CA, USA.

[10]Immunology Graduate Program, Stanford University School of Medicine, Stanford, CA, USA.

[11]Department of Chemical & Systems Biology, Stanford University School of Medicine, Stanford, CA, USA.

[12]Department of Chemistry, Stanford University School of Medicine, Stanford, CA, USA.

[13]Howard Hughes Medical Institute, Stanford University, Stanford, CA, USA.

[14]Gladstone-UCSF Institute of Genomic Immunology, San Francisco, CA, USA.

[15]Stanford Cancer Institute, Stanford University School of Medicine, Stanford, CA, USA.

[16]Parker Institute for Cancer Immunotherapy, San Francisco, CA, USA.

[17]These authors contributed equally: Nathaniel W. Mabe, Min Huang.

[18]These authors jointly supervised this work: Kimberly Stegmaier, Robbie G. Majzner.

Abstract

Immunotherapy with anti-GD2 antibodies has advanced the treatment of children with high-risk neuroblastoma, but nearly half of patients relapse, and little is known about mechanisms of resistance to anti-GD2 therapy. Here, we show that reduced GD2 expression was significantly correlated with the mesenchymal cell state in neuroblastoma and that a forced adrenergic-to-mesenchymal transition (AMT) conferred downregulation of GD2 and resistance to anti-GD2 antibody. Mechanistically, low-GD2-expressing cell lines demonstrated significantly reduced expression of the ganglioside synthesis enzyme *ST8SIA1* (GD3 synthase), resulting in a bottlenecking of GD2 synthesis. Pharmacologic inhibition of EZH2 resulted in epigenetic rewiring of mesenchymal neuroblastoma cells and re-expression of *ST8SIA1*, restoring surface expression of GD2 and sensitivity to anti-GD2 antibody. These data identify developmental lineage as a key determinant of sensitivity to anti-GD2 based immunotherapies and credential EZH2 inhibitors for clinical testing in combination with anti-GD2 antibody to enhance outcomes for children with neuroblastoma.

Neuroblastoma, a malignancy arising from primitive neural crest cells of the developing autonomic nervous system, is the most common extracranial solid tumor of childhood and accounts for approximately 10% of pediatric cancer deaths[1]. Adoption of intensified, multimodal therapy has resulted in improvements in survival for children diagnosed with high-risk neuroblastoma[2]. In particular, the adoption of anti-GD2 antibody into upfront treatment protocols has reduced relapse rates, resulting in significantly improved overall survival. However, many patients still relapse despite anti-GD2 therapy, and mechanisms of resistance to anti-GD2 are poorly understood[3–5].

During development, multipotent precursor cells demonstrate epigenetic heterogeneity that dictates differentiation at critical junctions of lineage commitment. Progenitor cells of the autonomic nervous system commit to adrenergic or mesenchymal tissues depending on the expression of key transcription factors PHOX2B or PRRX1, respectively[6].

In neuroblastomas, tumor cells can co-opt these divergent, lineage-specific epigenetic programs to induce intratumoral heterogeneity and drive therapeutic resistance[7,8]. *PRRX1* expression is associated with mesenchymal tumors, and *PRRX1* overexpression is sufficient to induce an adrenergic-to-mesenchymal transition (AMT), highlighting neuroblastoma intrinsic transcriptional plasticity[7,8]. Mesenchymal signatures are enriched in relapsed human neuroblastoma tumors, suggesting that an altered lineage-dependent epigenetic state underlies resistance to therapeutic interventions in this disease[9].

GD2 is a disialoganglioside that is synthesized from ceramide via a complex pathway involving the activity of sialyltransferases and glycosyltransferases[10]. GD2 has been proposed to play roles in suppressing the immune system[11], as well as in metastatic progression[12], but despite being expressed on almost all neuroblastoma tumors[13], its mechanism of regulation is poorly understood.

Recent publications suggest that GD2 expression is heterogeneous in neuroblastoma[14–16]. Antigen remodeling through downregulation or complete loss of expression is a common form of resistance to immunotherapies[17–22]. Emerging data suggest that GD2 density may predict response to anti-GD2 containing therapies[11,15,23,24], but the mechanisms by which neuroblastoma tumor cells downregulate GD2 to avoid immune detection remain undefined.

In light of these studies, we evaluated whether tumor heterogeneity arising from lineage-specific transcriptional states correlates with GD2 expression and response to anti-GD2 therapy. Transcriptional rewiring via an AMT promoted GD2 loss through downregulation of the sialyltransferase GD3 synthase (GD3S; *ST8SIA1*), resulting in a bottleneck in the synthesis and expression of GD2 and abrogation of the efficacy of anti-GD2 antibodies. Inhibition of the H3K27me3 histone methyltransferase EZH2 with the US Food and Drug Administration (FDA)-approved drug tazemetostat, however, reprogrammed cells to a state associated with adrenergic features, reestablishing expression of *ST8SIA1* and GD2, thereby restoring sensitivity to anti-GD2 antibodies. These data define cell lineage as a key predictor of GD2 expression in neuroblastoma. Moreover, we demonstrate that EZH2 inhibition can result in epigenetic rewiring of mesenchymal neuroblastoma, a maneuver that could reestablish therapeutic efficacy of anti-GD2. These studies nominate EZH2 inhibition combined with anti-GD2-based immunotherapy regimens as a promising approach to overcome resistance and improve responses in patients with neuroblastoma and potentially other $GD2^+$ malignancies.

Results

Low GD2 expression is associated with AMT in vitro.

We cataloged GD2 expression for 23 neuroblastoma cell lines representative of the diversity of well-known genetic alterations in neuroblastoma (including *MYCN* amplifications, *ALK* mutations, *NRAS* mutations and arm-level copy alterations). Approximately half of neuroblastoma cell lines expressed GD2 ($n = 12$) on at least 50% of cells; however, a substantial number of cell lines were GD2 negative ($n = 11$) (Fig. 1a and Extended Data Fig. 1a). To evaluate transcriptional pathways differentially expressed between GD2-high and GD2-low cell lines, we mined publicly available RNA-sequencing data for 14 of the

cell lines found in the Cancer Cell Line Encyclopedia (CCLE) database. The cell lines were binned into either $GD2^+$ ($n = 7$) or $GD2^-$ ($n = 7$) groups, and two-class differential gene expression analysis was performed. Gene set enrichment analysis (GSEA) revealed that low GD2 expression is most significantly correlated with the 'HALLMARKS OF EMT' (Supplemental Table 1) gene set. These data suggested that GD2-low cells may enrich for the mesenchymal neuroblastoma epigenetic program. GSEA was then performed on a 485-gene signature identified as a core transcriptional program of the mesenchymal neuroblastoma lineage and a 369-gene signature identified as core transcriptional program of the adrenergic neuroblastoma tumor lineage[8]. We found that GD2-low cell lines were strongly correlated with a mesenchymal signature, and GD2-high cell lines were highly correlated with an adrenergic signature (Fig. 1b,c).

To identify whether all GD2-low cell lines are bona fide mesenchymal cell lines, we generated adrenergic (ADRN) and mesenchymal (MES) scores based on the lineage signatures for all expression data available from the CCLE (Extended Data Figs. 1b,c). Among cell lines found in the CCLE, we identified 5 mesenchymal cell lines and 23 adrenergic cell lines. Intersection of cell state designations with the GD2 profiling identified that all 5 mesenchymal cell lines were GD2-low, whereas only 2 of the 9 adrenergic cell lines were GD2-low (Extended Data Fig. 1d). Thus, neuroblastomas co-opt divergent, lineage-related transcriptional programs that are correlated with altered GD2 expression.

We next evaluated the relationship between SH-EP and SH-SY5Y cell lines, which are derived from the same parent SK-N-SH culture but express a mesenchymal and adrenergic gene expression program, respectively (Extended Data Fig. 1e)[25]. The mesenchymal SH-EP cell line expressed little-to-no detectable surface GD2, whereas the adrenergic SH-SY5Y cell line demonstrated robust GD2 expression (Fig. 1d). These data suggest that GD2 expression is closely related to an adrenergic versus mesenchymal cell lineage.

To demonstrate that decreased GD2 expression in cell line models confers reduced sensitivity to anti-GD2 therapy, SH-EP and SH-SY5Y cells were co-cultured with either macrophages or $CD16^+$ natural killer (NK) cells (Extended Data Fig. 1f) in the presence or absence of dinutuximab, an FDA-approved anti-GD2 antibody. Macrophage phagocytosis and NK-mediated tumor cell killing were significantly greater for the GD2-high SH-SY5Y versus GD2-low-SH-EP cell lines (Fig. 1e and Extended Data Fig. 1g). These data suggest that cell state is correlated with expression of GD2 and response to anti-GD2-based therapies in neuroblastoma.

Low GD2 expression is associated with AMT in vivo.

To establish whether transcriptional heterogeneity can drive outgrowth of GD2-low cells, NSG mice were engrafted with the Kelly cell line and treated with dinutuximab. Kelly cells were chosen due to the heterogenous expression of GD2 (Fig. 1a). Anti-GD2 therapy significantly reduced tumor growth (Fig. 1f) but drove outgrowth of GD2-low-expressing tumor cells (Fig. 1g). To understand transcriptional programs that underlie GD2 expression, parental Kelly cells were sorted by fluorescence-activated cell sorting (FACS) into GD2-low (Kelly-$GD2^{low}$) and GD2-high (Kelly-$GD2^{high}$) populations (Extended Data Fig. 2a). The Kelly-$GD2^{high}$ cells showed greater sensitivity to anti-GD2 in combination with either

macrophages or NK cells (Extended Data Fig. 2b,c). RNA-sequencing analysis revealed that Kelly-GD2^{low} cells are enriched for mesenchymal-like signatures and express elevated CD133 (PROM1) by flow cytometry, a cell surface protein associated with undifferentiated and mesenchymal subpopulations in neuroblastomas (Fig. 1h and Extended Data Fig. 2d)[8,26]. Taken together, these data suggest that dinutuximab can drive outgrowth of GD2-low tumor cells within a heterogenous population, selecting for GD2-low cells that are associated with a MES-like gene signature.

Induction of AMT is sufficient to drive loss of GD2 expression.

We next wanted to develop tools to directly test whether the AMT is sufficient to downregulate GD2 expression in isogenic models. The paired-homeobox transcription factor PRRX1 has been proposed as a master transcription factor that regulates mesenchymal switch in neuroblastoma[7,8]. We infected two neuroblastoma cell lines (SK-N-BE(2) and KP-N-YN) with a doxycycline-inducible *PRRX1* conjugated to hemagglutinin (HA) (PRRX1-HA). These cell lines were chosen due to their adrenergic transcriptional program and high expression of GD2. Upon PRRX1 induction, both cell lines underwent a phenotypic conversion evidenced by upregulation of the mesenchymal markers fibronectin, YAP1, TAZ and vimentin and downregulation of the adrenergic marker PHOX2A (Fig. 2a). RNA sequencing showed profound transcriptional alterations in SK-N-BE(2) (710 genes decreased and 2,274 genes increased expression) and KP-N-YN (2,935 genes decreased and 3,147 genes increased expression) in response to PRRX1 overexpression (Fig. 2b). These transcriptional alterations showed that adrenergic genes were significantly downregulated and mesenchymal genes were significantly upregulated, consistent with an AMT (Fig. 2b and Extended Data Fig. 3a). Transcriptional rewiring resulted in dramatically decreased surface GD2 expression (Fig. 2c,d), reducing the therapeutic response to dinutuximab by both macrophages and NK cells (Fig. 2e,f and Extended Data Fig. 3b). In an orthogonal model, we overexpressed the intracellular portion of NOTCH3 (NOTCH3^{IC})[27] and observed an induction of AMT in SK-N-BE(2) cells. Similar to PRRX1 overexpression, NOTCH3^{IC} mediated induction of AMT and reduced GD2 expression (Extended Data Fig. 3c–e). These data offer direct evidence that rewiring of cell state directly alters GD2 expression and drives resistance to anti-GD2 antibody.

Low *ST8SIA1* expression is a bottleneck to GD2 synthesis.

We next sought to identify the genes or pathways that explain the downregulation of GD2. We correlated the percentage of GD2^{+} cells with gene expression for all genes in the CCLE database. We found that among the most correlated genes with surface GD2 expression was *ST8SIA1* (correlation = 0.89; R^2 = 0.79; *P* value < 0.001) (Fig. 3a and Supplemental Table 2). GD2 is synthesized from ceramide by a network of sialyltransferases and glycosyltransferases (Fig. 3b and Extended Data Fig. 4a)[10]. The *ST8SIA1* gene encodes for GD3S, which converts GM3 to GD3 (ref. [28]). GD3 is subsequently converted to GD2 by *B4GALNT1* (GD2 synthase; GD2S). Surprisingly, expression of *B4GALNT1* did not strongly correlate with GD2 expression, despite the requirement of that enzyme to generate GD2 (correlation = 0.345; R^2 = 0.12; *P* value = 0.25) (Fig. 3c). In fact, no enzymes in the ganglioside synthesis pathway other than *ST8SIA1* were strongly correlated with GD2 expression (Fig. 3d). We confirmed by messenger RNA (mRNA) that *ST8SIA1* expression

was significantly reduced in GD2-low versus GD2-high cell lines, whereas *B4GALNT1* showed heterogenous expression that was not correlated with GD2 expression (Fig. 3e,f). Consistent with the loss of *ST8SIA1* in cell line models, comparison of expression for enzymes in the ganglioside synthesis pathway between isogenic Kelly-GD2^{low} and Kelly-GD2^{high} cells showed highly reduced expression of *ST8SIA1* as well as a much smaller magnitude change in *ST3GAL5* (GM3 synthase) in Kelly-GD2^{low} versus Kelly-GD2^{high} cells (Fig. 3g). We sorted two additional cell lines, SH-EP (majority GD2-low) and CHLA-255 (GD2-heterogenous), into GD2^{low} and GD2^{high} populations (Extended Data Fig. 4b). SH-EP-GD2^{low} cells showed an over 20-fold reduction in expression of *ST8SIA1* and no change in expression of *B4GALNT1* or *ST3GAL5* as compared to SH-EP-GD2^{high} cells. Similarly, isogenic CHLA-255-GD2^{low} cells showed a nearly 20-fold reduction in expression of *ST8SIA1* but only a twofold reduction of *B4GALNT1* and a small reduction in expression of *ST3GAL5* as compared to CHLA-255-GD2^{high} cells (Extended Data Fig. 4c). Taken together, these data suggest that *ST8SIA1* is correlated with the loss of surface GD2 expression.

ST8SIA1 overexpression restores responsiveness to anti-GD2 antibody.

Given that GD3S is strongly correlated with surface GD2 expression, we next evaluated whether GD3S re-expression alone is sufficient to restore GD2 levels. We transduced three GD2-low cell lines (Kelly-GD2^{low}, NB-SD and SK-N-AS) with genes encoding GD3S alone, GD2S alone or both genes in combination and evaluated the effect on GD2 expression (Fig. 3h). We specifically chose an adrenergic cell line (NB-SD), a mesenchymal cell line (SK-N-AS) and the sorted Kelly-GD2^{low} cell line to represent heterogeneity in neuroblastoma cell lineages. Overexpression of GD3S alone resulted in significant enhancement of GD2 expression in all lines, whereas GD2S overexpression was insufficient to drive GD2 expression in any of these cell lines. Even in the setting of overexpressed GD3S, GD2S overexpression did not result in any further increase in GD2 expression in two of the three cell lines (Kelly-GD2^{low} and NB-SD) and resulted in slightly enhanced GD2 expression in SK-N-AS (Fig. 3h). Overexpression of GD3S alone was sufficient to restore sensitivity to anti-GD2 antibody (Fig. 3i and Extended Data Fig. 4d). Additionally, overexpression of *ST3GAL5* (GM3 synthase) failed to induce GD2 expression in these models (Extended Data Fig. 4e), suggesting that *ST8SIA1* is the critical bottleneck to the production of GD2 in neuroblastoma cells.

GD3S expression is correlated with the AMT lineage switch.

We next evaluated whether GD3S expression is correlated with the AMT lineage switch. First, we correlated *ST8SIA1* expression against all genes for neuroblastoma cell lines in the CCLE, independent of GD2 expression, and performed GSEA. We found that *ST8SIA1* expression was strongly enriched in the adrenergic subtype and negatively associated with the mesenchymal signature (Fig. 4a,b). Consistent with this finding, mesenchymal neuroblastoma cell lines from the CCLE showed significantly lower expression of *ST8SIA1* but not *B4GALNT1* (Fig. 4c). Further, we observed significantly reduced *ST8SIA1* mRNA and GD3S protein in the two models of AMT and in GD2-low SH-EP versus GD2-high SH-SY5Y cells (Fig. 4d,e and Extended Data Fig. 4f). Overexpression of *ST8SIA1*/GD3S resulted in dramatic upregulation of surface GD2 and restored sensitivity to anti-GD2

therapy in PRRX1-induced cell lines (Fig. 4f,g). Taken together, multiple independent mesenchymal models strongly demonstrate that AMT is associated with low expression of *ST8SIA1* (GD3S), which is consistently correlated with low GD2 surface expression by tumor cells.

We next evaluated whether *ST8SIA1* expression correlates with the mesenchymal lineage in human neuroblastoma tumors. Mesenchymal and adrenergic gene expression scores were calculated for 201 neuroblastoma tumors from the TARGET and Treehouse datasets to define the predominant lineage state of each tumor (Fig. 5a). A total of 172 adrenergic and 29 mesenchymal tumor designations were overlaid onto uniform manifold approximation and projection (UMAP) projections of global RNA sequencing from the Broad Institute's Celligner tool[29]. This UMAP clusters tumors and subtypes based on global transcriptional similarity for all tumor types (Extended Data Fig. 5). For neuroblastoma, we observed several mesenchymal-like tumors that cluster separately from the bulk of adrenergic tumors (Fig. 5b). Mesenchymal cell lines (for example, SK-N-AS) also cluster within the mesenchymal-like tumors, suggesting robust identification of mesenchymal neuroblastoma tumors. Comparison of gene expression between adrenergic and mesenchymal tumors from TARGET and Treehouse datasets revealed that mesenchymal-like tumors have significantly reduced expression of *ST8SIA1* (Fig. 5c,d). Consistent with this finding, in a complementary dataset of 579 neuroblastoma tumors[9], we found significantly decreased *ST8SIA1* in mesenchymal-like tumors (Fig. 5e). In both datasets, there was a more modest decrement in *B4GALNT1* expression in the mesenchymal tumors (Figs. 5c,e). Gartlgruber et al. characterized a matched primary and relapsed neuroblastoma tumor pair that showed decreased expression of adrenergic genes (for example, *PHOX2B*), increased mesenchymal genes (for example, *PRRX1* and *VIM*) and lower *ST8SIA1* mRNA in the mesenchymal-like relapsed sample (Fig. 5f)[9]. These data suggest that mesenchymal-like tumors express lower *ST8SIA1*, which determines surface GD2 expression and could play a role as a biomarker of response to anti-GD2 immunotherapy.

EZH2 inhibition rewires lineage plasticity and increases GD2.

Given the relationship of GD2 expression with the differentiation state of neuroblastoma cells, we sought to better understand epigenetic regulation of the *ST8SIA1* promoter. We mined publicly available chromatin immunoprecipitation (ChIP)-sequencing datasets for the presence of the active histone mark H3K27ac and the repressive histone mark H3K27me3 in two GD2-high cell lines (NB-69 and LAN-5) and two GD2-low cell lines (SK-N-AS and SK-N-BE(2)-C)[30] (Fig. 1a and Extended Data Fig. 6a). Analysis of the GD2-high cell lines NB-69 and LAN-5 revealed that the *ST8SIA1* promoter is enriched for the active H3K27ac mark, whereas levels of the repressive H3K27me3 mark are low (Extended Data Fig. 6b). In contrast, the two GD2-low cell lines, SK-N-AS and SK-N-BE(2)-C, demonstrated high H3K27me3 and low H3K27ac levels at the *ST8SIA1* promoter.

H3K27me3 deposition is mediated through the catalytic EZH2 subunit of the PRC2 protein complex and is thought to repress gene expression by compacting chromatin[31]. PRC2 plays an important role in maintaining cell identity, such as during neural crest differentiation and during proliferation[32]. A report in Ewing sarcoma suggests that EZH2 inhibitors may boost

GD2 expression in part through upregulation of GD3S[33] and thus may have therapeutic benefit in neuroblastomas as well. Furthermore, EZH2 inhibitors have been shown to induce neuronal differentiation and apoptosis in neuroblastomas[34–36]. Thus, we hypothesized that PRC2 inhibition may be a useful approach to upregulate GD2 expression in neuroblastoma.

Tazemetostat (EPZ-6438) is currently the only FDA-approved EZH2/PRC2 inhibitor. Prolonged treatment of the mesenchymal, GD2-low SK-N-AS cell line with tazemetostat resulted in a concentration-dependent increase in GD2 (Fig. 6a,b and Extended Data Fig. 6c). Further, EZH2 inhibition resulted in loss of the repressive H3K27me3 mark and gain of active H3K4me3 mark at the *ST8SIA1* promoter by ChIP-qPCR (Fig. 6c) and significant upregulation of *ST8SIA1* mRNA (Fig. 6d). We extended these results by treating the Kelly-GD2^{low}, CHLA-255-GD2^{low} and the adrenergic, GD2-low NB-SD cell lines with tazemetostat. Similar to the effects of EZH2 inhibition in SK-N-AS cells, GD2 cell surface levels were increased in Kelly-GD2^{low}, CHLA-255-GD^{low} and NB-SD cell lines and was associated with increased *ST8SIA1* mRNA (Fig. 6a,b,d and Extended Data Fig. 6d,e). We extended our findings to validate that EZH2 inhibition increased GD2 in three Ewing sarcoma cell lines and two small cell lung cancer cell lines, as has been shown previously (Extended Data Fig. 6f)[33,37]. Therefore, EZH2 inhibitors may be broadly used to enhance GD2 across tumor lineages.

SK-N-AS cells that were treated with tazemetostat and then incubated with human macrophages in the presence of dinutuximab were significantly more likely to be phagocytosed than those treated with vehicle (Fig. 6e). The upregulation of GD2 persisted at least 28 days after tazemetostat withdrawal, suggesting that the GD2 upregulation is mediated through transcriptional reprogramming that is durable for some period of time (Extended Data Fig. 6g).

Given that GD2 expression is correlated with lineage plasticity, we hypothesized that EZH2 inhibition leads to GD2 upregulation in part through lineage switching of the mesenchymal cell state to an adrenergic/neuronal transcriptional program. To answer this question, we performed assay for transposase-accessible chromatin (ATAC) sequencing, RNA sequencing and ChIP sequencing for H3K27me3 in the mesenchymal cell line SK-N-AS treated with tazemetostat for 21 days. Tazemetostat resulted in significantly reduced genome-wide H3K27me3 occupancy (Extended Data Fig. 7a,b). Increased RNA expression by RNA sequencing was associated with loss of H3K27me3 chromatin occupancy by ChIP sequencing and with increased chromatin accessibility by ATAC sequencing (Extended Data Fig. 7c,d). RNA sequencing revealed a significant enrichment for the adrenergic transcriptional program with EZH2 inhibition by GSEA analysis, and this enrichment was accompanied by increased expression of proteins in the adrenergic gene set (Fig. 6f,g). Among the most upregulated adrenergic genes, a subset of 45 consensus adrenergic genes showed both dramatically reduced H3K27me3 occupancy and increased chromatin accessibility with tazemetostat treatment (Fig. 6h,i). These 45 genes include known regulators of neuronal differentiation, such as *ASCL1*, *DLK1*, *INSM1*, *CHGA* and *LMO3* (Supplemental Table 3). Tazemetostat is also expected to induce numerous epigenetic effects aside from adrenergic differentiation. We observed a total of 575 genes with reduced H3K27me3 signal that were significantly upregulated by RNA and

rendered more accessible by ATAC sequencing (Extended Data Fig. 7e). Hypergeometric overlapping analysis revealed that these epigenetically regulated genes are enriched for known pathways modulated by EZH2 inhibition such as neuronal differentiation and PRC2 signatures (Extended Data Fig. 8). In addition, we observed non-lineage-related upregulation of pathways involving cell migration/adhesion, extracellular matrix and ion/nutrient transport (Supplemental Table 4). Importantly, the *ST8SIA1* gene is within this 575 epigenetically regulated gene set ($\Delta \log_2$ area under the curve (AUC)[H3K27me3] = −4.98, Δ log2AUC[ATAC] = 1.76, $\log_2$ fold change RNA = 7.2; Fig. 6j and Supplemental Table 3). Taken together, these data suggest EZH2 inhibitors can induce an adrenergic gene expression program in neuroblastomas with mesenchymal lineage and increase *ST8SIA1* expression, thereby increasing GD2 expression and response to anti-GD2 antibodies.

EZH2 inhibition improves response to anti-GD2 in vivo.

We next evaluated whether pharmacologic inhibition of EZH2 is effective to increase GD2 expression in vivo. As single agents, anti-GD2 antibodies are most effective on minimal residual disease and microscopic dissemination of neuroblastoma tumor cells[38]. We injected GD2-low mesenchymal SK-N-AS cells expressing luciferase into the tail vein of NSG mice to model disseminated disease and observed an over 800-fold increase in GD2 expression with tazemetostat treatment alone in SK-N-AS cells (Fig. 7a). Similar effects of tazemetostat treatment on GD2 expression were observed in an additional metastatic model of neuroblastoma using the GD2-heterogenous parental Kelly cell line and in an orthotopic model of osteosarcoma (MG63.3) (Extended Data Fig. 9a–d).

We next tested the efficacy of combining tazemetostat with anti-GD2 antibody in mesenchymal SK-N-AS tumors. Anti-GD2 alone was completely ineffective in this GD2-low mesenchymal model, but epigenetic reprogramming with tazemetostat enabled dinutuximab binding, resulting in significantly diminished tumor burden (Fig. 7b–d). Tumors that grew out in mice receiving dinutuximab and tazemetostat demonstrated lower and heterogenous expression of surface GD2 and *ST8SIA1* expression, although these tumors were obtained at disease endpoint multiple days after treatment withdrawal (Fig. 7e,f and Extended Data Fig. 9e). These data indicate that inhibition of EZH2 is a promising mechanism to enhance the efficacy of anti-GD2 antibody-based regimens and should be rapidly translated to the clinic.

EZH2 inhibition is reported to have effects on immune cell function and development, including NK cells and macrophages[39–41]. However, we observed only minimal alterations in tumor associated murine myeloid populations with tazemetostat treatment (Extended Data Fig. 10a) and no alterations in macrophage polarization (Extended Data Fig. 10b), indicating that tazemetostat did not result in significant changes to the immune effector cells in our model. To exclude the effect of EZH2 on myeloid cell function, we pretreated SK-N-AS cells with tazemetostat before testing GD2-based immunotherapies in the mouse model. EZH2 inhibitor pretreatment resulted in significantly reduced tumor growth in response to both anti-GD2 antibody and anti-GD2 chimeric antigen receptor (CAR) T cells (Fig. 7g) and no growth difference in the absence of anti-GD2 treatment. In both experiments, tumor cells that survived treatment were GD2 negative (Extended Data Fig. 10c). These data

indicate that EZH2 inhibitors may prevent neuroblastoma cells from using lineage plasticity to escape immunotherapy and could be effectively combined with anti-GD2 antibody to enhance their effects.

Patients receiving anti-GD2 antibodies develop a painful neuropathy/allodynia during infusion due to on-target, off-tumor binding of GD2 expressed by normal peripheral nerves. We tested whether EZH2 inhibition would inadvertently increase GD2 expression on healthy nerve tissue. First, we treated early-passage primary human cortical neurons (HCN-001) expressing low-to-moderate levels of GD2 with tazemetostat and observed a minimal increase in GD2 by flow cytometry or immunofluorescence (Fig. 8a,b and Extended Data Fig. 10d). We also observed no overt increase in GD2 expression by immunohistochemistry in cortical brain tissue from mice treated for at least 21 days with tazemetostat (Fig. 8c). Finally, we treated induced neurons from human embryonic stem cells (hESCs) that express high GD2 with tazemetostat and observed no further increase in GD2 expression by immunofluorescence or flow cytometry (Extended Data Fig. 10e,f). These data indicate that inhibition of EZH2 is a promising mechanism to enhance the efficacy of anti-GD2 antibody-based regimens and should be evaluated in clinical trials.

Discussion

In the present study, we demonstrate that lineage plasticity is a key regulator of GD2 expression in neuroblastoma which determines response to anti-GD2 antibody. Differential gene expression analysis following GD2 profiling in a large cohort of neuroblastoma cell lines showed marked enrichment for a mesenchymal signature in GD2-low cell lines. Mesenchymal cell lines express lower levels of GD2 antigen through EZH2-dependent regulation of the upstream catalytic enzyme *ST8SIA1* (GD3S). Inhibition of EZH2 restored expression of GD3S and sensitivity to dinutuximab both in vitro and in vivo, underscoring a combinatorial pharmacologic strategy to enhance responsiveness to anti-GD2 therapy in the clinic (schema in Fig. 8d).

Our data provide evidence that tumor cell heterogeneity can drive resistance to anti-GD2 therapy through enrichment of mesenchymal cell populations. Neuroblastoma relapses have been associated with enrichment of mesenchymal-like cells, and relapsed neuroblastomas have been shown to have mutations in genes such as *RAS* that promote mesenchymal-related processes[8,9,42]. Chromatin remodeling has also been associated with resistance to chemotherapeutics and targeted therapies in vitro[8,43]. Importantly, although we establish the mesenchymal state is one mechanism underlying low GD2 expression, some adrenergic lineage cell lines also demonstrate low GD2 expression, suggesting that alternate nonlineage pathways may also regulate GD2 expression.

Our data identify a strong link between *ST8SIA1* mRNA and GD2 expression in both mesenchymal and adrenergic neuroblastoma. Many studies have used the expression of *B4GALNT1* as a potential biomarker for GD2 expression in neuroblastoma cells[44–46]. However, we showed through extensive in vitro testing that *B4GALNT1* expression does not correlate with GD2 expression, nor does *B4GALNT1* overexpression rescue downregulation of GD2 expression in GD2-low neuroblastoma cells. Thus, we posit GD3S as an important

indicator of GD2 expression and potential response to anti-GD2 therapies. Interestingly, patient tumors with greater enrichment for mesenchymal signatures express significantly lower GD3S expression, suggesting that AMT could be an important mechanism underlying resistance to anti-GD2. Staining for GD2 expression on formalin-fixed tissues is unreliable, and therefore, GD2 is rarely assessed on primary neuroblastoma tumors. Thus, whether *ST8SIA1* expression correlates with GD2 in patient samples remains unknown and will be paramount to establishing GD3S as a potential biomarker for response to anti-GD2 in patients.

The existence of tumor cells resembling mesenchymal-like programs in human patients is under intense investigation. Although we found evidence of primary neuroblastoma tumors with mesenchymal-like transcriptional programs that overlap bona fide mesenchymal cell lines, these tumors may demonstrate mixed mesenchymal transcriptional programs. Recently, single-cell RNA-sequencing studies show mixed results regarding whether mesenchymal tumor cells exist in tumors[47,48]. Likely, mesenchymal tumor cells resemble Schwann cell precursors of the developing neural crest and are enriched in relapsed tumors[9], underlying the importance of lineage plasticity in therapy resistance. This mechanism of resistance is also observed in adult malignancies, such as lung and prostate cancers, where epigenetic plasticity is commonly seen in response to chemotherapy and targeted therapies[49,50]. Additional studies evaluating the effect of neuroblastoma treatment regimens on mesenchymal transition and GD2 expression in patients will be important to establish the role of lineage switch in driving resistance to anti-GD2.

EZH2 inhibitors have been studied for their ability to induce neuronal differentiation in preclinical models of neuroblastoma and are effective across numerous subtypes[35,36]. Negative regulation of EZH2 activity, such as through miR-124 expression, has also been shown as critical for regulating cell state and differentiation in neuroblastoma[51]. We showed that the FDA-approved EZH2 inhibitor tazemetostat reprogrammed the cell state in mesenchymal neuroblastoma, inducing an adrenergic gene expression signature that resulted in upregulation of GD2, restoring sensitivity to anti-GD2 antibody. This finding reflects similar biology that we previously reported in H3K27M mutant gliomas, where GD2 expression level is higher than other cancers due to persistent loss of histone-3 trimethylation associated with the driver mutation, resulting in preclinical and clinical efficacy of anti-GD2 CAR T cells[52,53]. Previous reports in neuroblastoma show that histone deacetylase inhibitors may also boost GD2 expression in part through upregulation of ganglioside synthesis enzymes[54,55].

Importantly, we demonstrate that EZH2 inhibition does not increase GD2 on the cell surface of healthy nervous system tissue, suggesting combinatorial therapy may not increase on-target, off-tumor toxicity of anti-GD2 therapies. Tazemetostat has been shown to be effective in adult epithelioid sarcomas and B cell non-Hodgkin lymphomas[56–58] and is being studied for safety in pediatric patients (NCT02601937). These data credential the combination of tazemetostat and anti-GD2-based regimens for testing in clinical studies. In conclusion, our data link expression of the critical GD2 synthesis enzyme GD3S (*ST8SIA1*) to lineage plasticity. This work suggests that altering the epigenetic cell state with EZH2 inhibitors

may enhance response to anti-GD2 therapy, thus improving outcomes for patients with advanced neuroblastomas.

Methods

Our research studies comply with ethical guidelines determined by the Stanford University Animal Care and Use Committee under protocol number 33698. Experimental endpoint was determined by reduced activity, swelling of the abdominal area and/or bioluminescence intensity (BLI) measurements above 1×10^{11} or tumor volume ≥15 mm in any direction. Maximum tumor burden was not exceeded in these experiments. Primary human tissue from the cortex and diffuse intrinsic pontine glioma tumor were obtained with patient informed consent on a Stanford University Institutional Review Board-approved protocol 14511. The patient was not compensated for this study. Further information on research design is available in the Nature Research Reporting Summary linked to this article.

Cell lines and reagents.

SK-N-DZ, SK-N-FI, SK-N-AS, SK-N-BE(2), SK-N-SH, NB-1, IMR-32, SIMA, Kelly, CHP-212, SK-PN-DW, EW-8, TC-32 and GI-M-EN cell lines were collected from the Cancer Cell Line Encyclopedia and Cancer Dependency Map projects and obtained from the Broad Institute. KP-N-SI9S and KP-N-YN were purchased from the Japanese Collection of Research Bioresources cell bank. SH-SY5Y, HEK293T and SK-N-BE(2)-C lines were purchased from ATCC. NB-69 cells were kindly gifted from T. Look's laboratory at Dana-Farber Cancer Institute (DFCI) and can be purchased from the European Collection of Authenticated Cell Cultures. LAN-1 and ACN were kindly gifted by R. George at DFCI and can be purchased from the European Collection of Authenticated Cell Cultures (LAN-1). SH-EP cell line was kindly gifted from M. Irwin's lab at SickKids. CHLA-255 and KCNR lines were obtained from R. Seeger at Children's Hospital Los Angeles and NB-SD from J. Maris at Children's Hospital of Philadelphia. CHLA-15 was obtained from the Children's Oncology Group. H-69 and H-82 were obtained from J. Sage's lab at Stanford. M63.3 was obtained from C. Khanna (National Cancer Institute). Primary human cortical neurons HCN-001 were purchased from NEUROMICS. SK-N-BE(2)-C, ACN, LAN-1, SK-N-FI, SK-N-AS, GI-M-EN, CHP-212, HEK293T, HEK293GP, SK-PN-DW and SH-EP cells were grown in 10% DMEM supplemented with glutamine, penicillin and streptomycin. Kelly, KP-N-SI9S, KP-N-YN, CHLA-255, KCNR, SK-N-DZ, SH-SY5Y, SK-N-BE(2), NB-1, NB-69, CHLA-15, NB-SD, EW-8, TC-32, H-69, H-82, MG63.3 and SIMA cells were grown in RPMI-1640 supplemented with 10% fetal bovine serum (FBS) and glutamine, penicillin and streptomycin. IMR-32 and SK-N-SH were grown in EMEM supplemented with 10% FBS and glutamine, penicillin and streptomycin. HCN-001 neurons were grown in Human Neuron Cells Growth medium (HNM 001) from NEUROMICS. Cell lines identities were validated by Short Tandem Repeat profiling and tested negative for mycoplasma with a Lonza mycoplasma detection kit (Lonza Mycoalert) before experimental use and used within 6 months of testing.

Flow cytometry.

Cell lines were trypsinized into suspension and washed twice with PBS + 2% FBS before staining with primary antibodies listed or isotype or secondary only antibodies as a control. Antibodies were incubated for 15–60 min at 37 °C. Cells were filtered through a 40-μM filter and immediately measured on a BD Celesta or Fortessa flow cytometer. Flow cytometry analysis was collected in BD FACSDIVA v9.0. Data analysis was performed in FlowJo (v10.6.1).

Representative gating strategies used in flow cytometry experiments can be found in Supplemental Figs. 1–7.

Western blotting.

Cell pellets were lysed with CS lysis buffer (9803) supplemented with phosphatase (Roche 04906845001) and protease inhibitors (11836170001) and diluted to 1 μg μl^{-1} in sample buffer. Histone extractions were performed according to standard protocol (Abcam). Approximately 35 μg whole-cell lysate protein or 2 μg of histones were loaded into wells and resolved in 4–12% acrylamide gradient gels. Whole-cell lysates and histone lysates were run with MOPS running buffer solution and MEPS running buffer solution, respectively. Acrylamide gels were wet-transferred onto nitrocellulose membranes for at least 90 minutes and verified for proper transfer with ponceau red stain. Primary antibodies listed were diluted in 3% BSA in Tris Buffered Saline with Tween (TBS-T) and incubated overnight at 4 °C. Secondary antibodies were diluted 1:5,000 in TBS-T and incubated at room temperature (RT) for 1 h. All membranes were imaged on LI-COR Odyssey infrared imaging system at 680 or 800 nm wavelengths and analyzed with ImageStudio Odyssey Lite Software (LI-COR) v5.2.5.

Immunohistochemistry.

For immunohistochemistry, mice were transcardially perfused with PBS and post fixed in 4% paraformaldehyde (PFA) overnight at 4°C. Brains were sunk in 30% sucrose and embedded in optimal-cutting temperature (OCT) compound (TissueTek). Primary samples from patients were transferred to cryomolds and embedded in OCT compound (TissueTek). Then, 10-μm cryosections were generated on a cryostat (Leica). Tissue was fixed with 4% PFA at 4 °C for 20 min and then washed, and endogenous peroxidase activity was neutralized (Bloxall, Vector Laboratories, 10 min at RT) before permeabilization (0.3% Triton X-100, Tris-buffered saline (TBS), 15 min at RT) and blocking (5% horse serum, Vector Laboratories, 20 min at RT). Tissue was stained with GD2 primary (14g2a, BD, 1:500, 4 h at RT), and signal was developed using a polymer-based alkaline phosphatase secondary antibody (ImmPRESS AP anti-mouse immunoglobulin G (IgG), Vector Laboratories, 30 min at RT) and blue alkaline phosphatase substrate (Vector Blue AP substrate kit, Vector Laboratories, 10 min at RT). Alkaline phosphatase development was quenched in TBS, and samples were mounted and imaged (Zeiss Imager.M2). For tumor-bearing positive controls, sequential double-staining immunohistochemistry was conducted for H3K27M (Abcam ab190631, 1:1,000, 1 h RT) and GD2 (14g2a, BD, 1:500, 4 h at RT). H3K27M was developed with a peroxidase secondary (ImmPRESS VR anti–rabbit IgG, Vector Laboratories, 30 min at RT) and DAB substrate (BD). After quenching the DAB

substrate development in TBS, and staining with the 14g2a primary antibody, GD2 signal was developed using an identical method as the mouse brains. Microscopy images were analyzed with Fiji (v2.1.0)

Plasmids and viral transduction.

Codon-optimized DNA fragments encoding *PRRX1*, *ST8SIA1* and *NOTCH3*^{IC} were purchased as a gBlock (IDT) and cloned into pDONR-221 via BP gateway cloning. *PRRX1* and *NOTCH3*^{IC} were further cloned into pINDUCER20 (Addgene, 44012) and *ST8SIA1* was further cloned into PLX307 (Addgene, 41392) via LR Gateway cloning. A *B4GALNT1* lentiviral vector and an additional *ST8SIA1* lentiviral vector were received from OriGene. High-titer lentivirus was produced by transfection of HEK293T cells with the lentiviral vector, psPAX2 (Addgene, 12260) and vsvg (Addgene, 8454) with Lipofectamine 2000 (Life Technologies, 11668027). Lentiviral supernatant was collected 48 h after transfection and filtered with 0.2-μm filters. Cells were transduced with virus in the presence of 5 μg ml^{-1} polybrene and selected in some cases with G418 (400 μg ml^{-1}), blasticidin (5 μg ml^{-1}) or puromycin (1 μg ml^{-1}) according to appropriate selection agent. A codon-optimized DNA fragment for *ST3GAL5* was cloned into the MSGV1 retroviral vector. Retroviral supernatant production and cell transduction were performed as previously described[59].

qPCR.

RNA was extracted from cells using the RNAeasy Mini Kit (Qiagen) and on-column DNA digestion according to the manufacturer protocol and cDNA was synthesized from 2 μg RNA with the ImProm II reverse transcription system (Promega) or cDNA-IV kit (Thermo Fisher Scientific). Gene expression was measured in some experiments using TaqMan probes to *ST8SIA1* and *B4GALNT1* by generating expression scores relative to standard curve and normalizing the expression to housekeeping genes *ACTB, GAPDH* or *18 S*. Gene expression for *ST3GAL5*, *ST8SIA1*, *B4GALNT1*, *B3GALT4* and *ST3GAL2* were measured with Applied Biosystems Power Up SYBR Green reagent (Thermo Fisher Scientific) with the primers listed in Supplemental Table 5 and analyzed using ΔΔCT method and plotted as a percentage of transcript compared to the relevant control group.

ChIP-qPCR and sequencing.

Histone ChIP sequencing was performed on 2×10^7 cells per reaction. Cells were crosslinked for 10 min in 1% formaldehyde and quenched in 0.20 M glycine for 5 min. Cells were lysed with SDS buffer supplemented with protease/phosphatase inhibitor cocktail and cell nuclei were pelleted. Nuclei pellets were resuspended in immunoprecipitation (IP) buffer and sheared for 15 min on a E220 Covaris sonicator (5% duty cycle, peak power 140 W, cycles per burst 200) at 4 °C. Input lysates were separated from IP lysates, and the IP lysates were incubated overnight at 4 °C with a previously prepared mixture of antibody loaded on protein A or G magnetic beads. Magnetic beads were washed twice with low-salt wash buffer, twice with high-salt wash buffer, twice with LiCl wash buffer and once with cold Tris + EDTA buffer. Washed DNA was eluted from beads with ChIP elution buffer. Input and IP samples were reverse crosslinked in high salt at 65 °C overnight. Uncrosslinked DNA was purified with solid-phase reversible immobilization beads and eluted for downstream analysis. Real-time quantitative RT-PCR for *ST8SIA1* was

performed using SYBR green (Bio-Rad) in combination with primers listed in Supplemental Table 5 and represented as percentage of input DNA. A gene desert on chromosome 12 (ActiveMotif) was included as a negative control for antibody enrichment. DNA samples for ChIP sequencing were submitted to the DFCI genomics core facility for library preparation and sequencing. DNA libraries were prepared with automated Swift S2 ligation chemistry and at least 80 million 50-bp reads were sequenced on a NovaSeq platform.

ChIP-sequencing data analysis was performed in alignment with the ENCODE Consortium standards (https://www.encodeproject.org/chip-seq/). All of the ChIP-sequencing datasets were aligned to the GRCh38/hg38 human genes and *Drosophila melanogaster* dm6 genes using bowtie2–2.3.5 with the standard options. PCR duplicates were removed with the Picard v2.18.2 MarkDuplicates tool[60]. The Active Motif Spike-in Normalization protocol was then applied to each hg38 sample by multiplying the human tag counts with the normalization factors derived from the uniquely mapped *Drosophila* reads as ratios between the sample with the lowest dm6 counts versus the dm6 counts for that sample.

Correlations for replicate samples were computed with the multiBamSummary and bamCorrelate tools available in deepTools v3.5.1 (ref. [61]) and visualized as dendrograms and in principal-component analysis plots. Replicate reads were merged for each condition. The merged reads for the two vehicle-treated replicates were labeled “SKNAS_H3K27me3_Veh” and similarly, the merged reads for the two tazemetostat-treated replicates were labeled “SKNAS_H3K27me3_EPZ.” The mapped reads for individual replicates and for merged samples were normalized in units of reads per kilobase per million (RPKM or rpm/bp) and coverage tracks for the RPKM signal were created as bigwig files for bins of size 20 bp using the bamCoverage tool available in deepTools.

Peak calling was performed against input control using MACS2 software[62], with the broad option and false discovery rate ≤0.01. AUC RPKM normalized signal across genomic regions was computed with the bwtool software[63]. Peaks with low AUC coverage (<300 RPKM) were disregarded, and the ENCODE blacklisted regions for hg38 were removed from each set of peak regions. Quality control tests for the mapped reads were performed by using the ChIPQC library available from Bioconductor v3.10 (ref. [64]). The peaks were annotated with the closest hg38 genes by using the chipseeker package available from Bioconductor[65].

The binding sites identified by MACS2 on merged reads were aggregated into consensus peaks per condition by requiring AUC binding signal >500 for each replicate. The consensus peaks for both conditions were merged into a high-confidence union peak set. A peak by sample counts matrix was created by counting the reads overlapping each peak with the multiBamSummary tool available from deepTools. The counts matrix was used to perform differential peak analysis in DESeq2. Differential binding across conditions was assessed based on the significance cutoffs $|\text{Delta}(\log_2(\text{AUC} + 1))| \geq 0.5$ and adjusted P value ≤ 0.10. Genome track files were created with the bamCoverage tool available in deepTools and visualized as heatmaps and metaplots created with the computeMatrix tool available in deepTools, and with the Integrative Genomic Viewer (v2.9.0).

RNA sequencing.

RNA was extracted from cells using the RNAeasy Mini Kit (Qiagen) according to the manufacturer's protocol. RNA was processed for quality control and integrity by Agarose gel electrophoresis and quantified with Agilent 2100. Samples were submitted to Novogene corporation for library preparation and sequencing for 150-bp paired-end reads on the NovaSeq platform. Sequencing depth varied between 35–50 million for each sample. Samples were trimmed of low-quality base pairs and adapters with trimmomatic package and processed for quality control with FastQC software. Processed reads were mapped to the GRCh38/hg38 human genome with STAR aligner and passed through featureCounts software to generate gene level reads. Differential gene expression analysis was determined with DESeq2 software. Volcano plots were generated in R (v.4.0.3) with ggplot2 software and heatmaps were generated with pheatmap package. Significance cut-offs were $\log_2$ fold change ≥ 1 and q-value ≤ 0.05.

ATAC sequencing.

ATAC-sequencing sample processing was performed according to the Omni-ATAC protocol[66]. Briefly, 50,000 cells per replicate were pelleted and then resuspended and lysed in 50 μl ATAC resuspension buffer supplemented with 0.1% NP40, 0.1% Tween-20 and 0.01% Digitonin. After lysis, nuclei were pelleted and transposed using 2.5 μl Tn5 transposase in a 50 μl reaction. Finally, the transposed DNA was purified using a commercial PCR cleanup kit, and libraries were amplified and prepared for sequencing. Paired-end sequencing (2 × 75) was performed on an Illumina NovaSeq.

ATAC-sequencing data analysis was performed in alignment with the ENCODE Consortium standards (https://www.encodeproject.org/atac-seq/). Briefly, the paired-end reads were trimmed and filtered using Trimmomatic v0.39 and mapped to the hg38 reference genome using bowtie2 with the –local –very sensitive –X 2,000 and MAPQ > 5 options. Bam files were deduplicated using Picard. Only reads with MAPQ > 5 and mapping to chromosomes 1–22 and chromosome X were retained. Reads were shifted with 4 bp on the positive strand and −5 bp on the negative strand using AlignmentSieve available in deepTools v3.5.1 (ref. [61]). Replicate correlations were computed with the multiBamSummary and bamCorrelate tools available in deepTools and visualized as dendrograms and in principal-component analysis plots. Fragment size distributions were computed with the bamPEFragmentSize tool available in deepTools. Properly aligned reads for replicates were merged for each condition.

The merged reads for the four vehicle replicates were labeled "SKNAS_ATAC_CTRL" and similarly, the merged reads for the four tazemetostat-treated replicates were labeled "SKNAS_ATAC_TAZE". The mapped reads for individual and merged replicates were normalized in units of RPKM (or rpm/bp) and coverage tracks for the RPKM signal were created as bigwig files for bins of size 20 bp by using the bamCoverage tool available in deepTools.

Peak calling was performed for properly aligned and for the merged reads with MACS2, with the –nomodel,–extsize to fragment length and –q 0.01 options. AUC binding signal for peaks was computed with the bwtool[63].

The binding sites identified by MACS2 (ref. [62]) on merged reads were aggregated into consensus peaks per condition by requiring AUC binding signal >1,000 for each replicate. The consensus peaks for both conditions were merged into a high confidence union peak set. A peak by sample counts matrix was created by counting the reads overlapping each peak with the multiBamSummary tool available from deepTools. The counts matrix was used to perform differential peak analysis in DESeq2. Differential binding across conditions was assessed based on the significance cut-offs $|\text{Delta}(\log_2(\text{AUC} + 1))| \geq 0.5$ and adjusted P value ≤ 0.10. Genome track files were created with the bamCoverage tool available in deepTools and visualized as heatmaps created with the computeMatrix tool available in deepTools and with the Integrative Genomic Viewer (v2.9.0).

Public datasets.

$\text{Log}_2(\text{TPM} + 1)$ RNA-sequencing data were downloaded from the Dependency Map portal (https://depmap.org/portal/, CCLE expression: 21Q1). Differential gene expression analysis between GD2-high and GD2-low populations was determined by two-class comparison analysis in the Dependency Map portal (https://depmap.org). Differential gene expression was input into GSEA (4.1.0) to determine gene set enrichments. For heatmaps, median-centered *z*-score normalized gene expression was using pheatmap. To determine the adrenergic and mesenchymal scores, average gene expression for each signature was used to calculate scores. Cutoffs for adrenergic or mesenchymal calls were determined by an average ADRN score ≤5 and an average MES score ≥4.1.

To determine the adrenergic and mesenchymal scores for TARGET and Treehouse tumors, TPM expression for neuroblastoma tumors was downloaded from the Tumor Compendium v11 Public PolyA (April 2020) on UCSC Treehouse genomics website (available at https://treehousegenomics.soe.ucsc. edu/public-data). Cutoffs were determined by an average ADRN score ≤5 and an average MES score ≥4.5. Projection of mesenchymal and adrenergic cell lines as compared to TARGET/Treehouse tumors was compared using UMAP projection plots generated by the Celligner alignment portal (available from https://depmap.org/portal/celligner, 21Q1). To determine the ADRN and MES scores for 579 tumors from Gartlgruber et al., TPM gene expression was downloaded from R2 (https://hgserver1.amc.nl/cgi-bin/r2/main.cgi) and single sample GSEA for MES and ADRN gene signatures were calculated for each tumor[9,67]. Mesenchymal tumors were defined as MES score ≥1.5 and ADRN score of ≤ −1.5, and adrenergic tumors were defined as an ADRN score ≥1.5 and MES score ≤−1.5.

ChIP-sequencing tracks for H3K27me3 and H3K27ac in neuroblastoma cell lines were downloaded from GSE138314[30] and visualized in IGV viewer (v2.9.0).

Macrophage phagocytosis assay.

Human blood-derived macrophages were generated from anonymous healthy donors as previously described[68]. Human blood samples were obtained through the Stanford Blood Center under an Institutional Review Board-exempt protocol. Tumor cells were labeled with CFSE (Invitrogen) as per the manufacturer protocol. Tumor cells were then incubated with the anti-GD2 antibody dinutuximab (obtained from Stanford pharmacy) at a concentration

of 10 μg ml^{-1} or media for 30 min at 37 °C. After incubation, tumor cells were washed twice in PBS and then co-cultured at a 2:1 ratio with macrophages in serum free media for 2 h at 37 °C. After co-culture, cells were washed with PBS and centrifuged at 1,200 × *g* for 5 min. They were then stained for downstream analysis with anti-CD11b (Clone M1/70, BioLegend) and Live/ Dead stain (Fixable Viability Dye, eBioscience). Flow cytometry was performed on an LRS Fortessa Analyzer (BD Biosciences), and phagocytosis was measured as the percentage of the total $CD11b^+$ macrophages that were also $CFSE^+$. Phagocytosis in response to dinutuximab was normalized to conditions without antibody.

NK co-culture assay.

NK cells were isolated from anonymous healthy donors via a CD3-depletion kit (Stem Cell Kit, Lymphoprep) and cultured in NK culture media (SCGM media with 10% FBS, 10 ng ml^{-1} interleukin-2 and 1% penicillin/streptomycin/glutamine). Human blood samples were obtained through the Brigham and Women's Hospital blood bank under an Institutional Review Board-exempt protocol. The presence of antibody-dependent cellular cytotoxicity-proficient NK cells was confirmed with CD16 expression by flow cytometry. NK cells were minimally passaged before plating. For 48-h co-cultures, 200–400 $\times 10^3$ tumor cells were plated on 12-well plates, and for 8-h co-cultures, 10,000 cells were plated per well on a 384-well plate. Wells received one of four treatment cohorts in triplicate (48 h) or quadruplicate (8 h): (1) human isotype antibody (1 μg ml^{-1}), (2) dinutuximab (1 μg ml^{-1}), (3) human isotype (1 μg ml^{-1}) with 1:2 (NK/tumor cell) ratio or (4) dinutuximab (1 μg ml^{-1}) with 1:2 (NK/tumor cell) ratio. For 8-h co-cultures, 10 μl CellTiter-Glo (Promega) reagent was added to wells and allowed to incubate for 15 min and measured on a spectrophotometer. Background from NK cells alone was subtracted from detected values, and treatments were normalized to cell viability in group 1. For 48-h co-cultures, cells were washed with PBS, trypsinized and counted in technical duplicate with trypan blue on a Countessa 2 cell counter and each of the three wells normalized relative to cell viability in group 1 (isotype without NK cells).

Neuronal differentiation of hESCs.

H1-ESCs (obtained from WiCell Research Resources) were maintained feeder-free in StemFlex medium (Gibco) and used at intermediate passage number (~50). ESC experiments were approved by the Stem Cell Research Oversight panel at Stanford University. Primary mouse glia cells were derived from the forebrain of newborn (post-natal day 2–3) wild-type C57BL/6 J mice. Briefly, forebrain homogenates were digested with Trypsin (Gibco) and cultured in DMEM (Gibco) supplemented with 10% cosmic calf serum (Hyclone), sodium pyruvate (Gibco), nonessential amino acids (Gibco), penicillin-streptomycin (Gibco) and 2-mercaptoethanol (Sigma-Aldrich). Glia cells were passaged multiple times before usage for co-culture experiments.

Induced neurons (iNs) were generated from H1-ESCs as previously described[69]. In short, H1-ESCs were detached with ACCUTASE (STEMCELL Technologies) and plated (~50,000 cells per cm^2) onto Corning Matrigel-coated plates in StemFlex medium (Gibco) supplemented with 2 μM Thiazovivin (Bio Vision) on day 0. Cells were transduced with lentiviral vectors FUW-rtTA (Addgene, 20342) and FUW-TetO-Ngn2- P2A-puromycin

(Addgene, 52047). Lentivirus was generated as previously described[70]. On day 1, culture medium was replaced with DMEM/F12 1:1 supplemented with N-2, nonessential amino acids, penicillin-streptomycin (all Gibco), insulin (12.5 μg ml^{-1}, Sigma) and doxycycline (2 μg ml^{-1}, Clontech) to induce gene expression. On days 2–4, puromycin (2 μg ml^{-1}, Sigma-Aldrich) was added to select for transduced cells. On day 4, AraC (4 μM, Sigma-Aldrich) was added to select for nondividing cells. For glia co-culture, iNs were detached with ACCUTASE (STEMCELL Technologies) and plated with primary mouse glia cells onto Corning Matrigel-coated coverslips on day 5. From day 5, cells were maintained in Neurobasal medium with B-27, Glutamax, penicillin-streptomycin (all Gibco) and either 2% FBS (Atlanta Biologicals) for iN–glia-co-culture or 0% FBS for iN monoculture.

Immunofluorescence staining of HCN-001 and hESC-iNs.

For immunofluorescence analysis, iN–glia-co-cultures were fixed with 4% PFA for 15 min and washed three times with PBS. Fixed cells were permeabilized and blocked with immunofluorescence buffer (PBS containing 0.3% Triton X-100 and 5% cosmic calf serum) for 1 h. Samples were incubated with primary antibodies in immunofluorescence buffer overnight at 4 °C and subsequently washed three times with PBS. Samples were then incubated with secondary antibodies for 1 h at RT and washed three times with PBS again. Cells were then incubated with 4,6-diamidino-2-phenylindole for 5 min at RT and washed two times with PBS. Coverslips were then mounted on glass slides with a ProLong Gold antifade reagent (Thermo Fisher Scientific). Images were obtained using Leica DM5500B and Leica DMi8 microscopes. Primary antibodies used for this study were anti-MAP2 (chicken, Abcam, ab5392) and anti-GD2 (mouse, BioLegend, 357302). Microscopy images were analyzed with Fiji (v2.1.0)

In vivo models.

For all in vivo experiments, immunodeficient NSG (NOD. Cg-Prkdcscid Il2rgtm1Wjl/SzJ) mice were ordered from the Jackson Laboratory or bred in-house and were between 6 and 12 weeks old at the start of experiments. Mice were housed with strictly controlled temperature and humidity and kept on 12-h light/dark cycles. An equal number of male and female mice were used between all experimental groups.

Kelly flank/dinutuximab resistance in vivo.

Kelly cells were expanded under standard culture conditions as described above. A total of 2×10^6 cells were resuspended in media without antibiotics or FBS and mixed at a 1:1 ratio with Matrigel (Corning) before being subcutaneously injected into unilateral flanks of eight NSG mice. Seven days after tumor engraftment, mice were randomized based on tumor size and treated with 300 μg anti-GD2 (dinutuximab, obtained from the Stanford Pharmacy) three times a week by intraperitoneal injection. Tumors were measured with digital calipers three times a week, and mice were euthanized when the majority of tumors reached the volume necessary to obtain enough tissue for GD2 detection by flow cytometry as described.

Combination tazemetostat and dinutuximab SK-N-AS in vivo metastatic model.

SK-N-AS cells expressing firefly-luciferase were expanded under standard culture conditions and resuspended in PBS before injection of 1×10^6 cells in 200 µl through the tail vein of 20 mice. Tumor growth was monitored by BLI on an IVIS Spectrum In Vivo Imaging System (PerkinElmer) 4 min after 3 mg d-luciferin (PerkinElmer) was injected intraperitoneally. BLI values were quantified with the Live Image v4.7.3 software (Living Image, PerkinElmer). Mice were randomized based on BLI and treatment was initiated seven days after tumor engraftment ($n = 5$ per treatment group). Treatment consisted of 300 µg anti-GD2 (dinutuximab, obtained from the Stanford Pharmacy) administered three times a week by intraperitoneal injection for 4 weeks with or without 500 mg kg^{-1} EPZ-6438 (Seleckchem) administered twice a day by oral gavage for 3 weeks. Experimental endpoint was determined by reduced activity, swelling of the abdominal area and/or BLI measurements above 1×10^{11} that triggered morbidity criteria for euthanasia. The formula for determining luminescence AUC was $[(lum_1 + lum_2)/2] - x\ (day_2 - day_1)$.

Immune cell populations from xenografted tumors were measured from untreated or tazemetostat-treated mice using primary antibodies. Macrophages were determined by the percentage of $CD11b^+$/ $F4/80^+$ in the $CD45^+$ population, M1 macrophages were determined by the percentage of $CD86^+$/ MHC-II $(I\text{-}A/I\text{-}E)^+$ cells in the macrophage population, M2 macrophages were determined by the percentage of $CD163^+$/ $CD206^+$ cells in the macrophage population, granulocytes were determined by the percentage of $CD11b^+$/ $Ly6G^+$ cells in $CD45^+$ cells, monocytes were determined by frequency of $CD11b^+$/ $Ly6C^+$ cells in $CD45^+$ cells and dendritic cells were determined by the frequency of CD11c MHC-II^+ in $CD45^+$ cells.

Tazemetostat-pretreated SK-N-AS in vivo metastatic model.

SK-N-AS cells expressing firefly-luciferase were pretreated in vitro with 1 µM tazemetostat (Seleckchem) for 3 weeks, and GD2 expression was confirmed by flow cytometry before 1×10^6 pretreated or control cells were injected in NSG mice through the tail vein of 30 mice. Mice were randomized based on BLI and treatment was initiated 4 days (dinutuximab) or 7 days (GD2-CAR) after tumor engraftment. Mice received either 300 µg anti-GD2 (dinutuximab, obtained from the Stanford Pharmacy) intraperitoneally three times a week or a single tail vein infusion of 1×10^7 GD2–4-1BBz CAR T cells ($n = 5$ per treatment group). Endpoint was determined as above or if mice showed clinical signs of graft versus host disease such as hair and weight loss (CAR T cell experiment only).

Tazemetostat in parental Kelly in vivo metastatic model.

Parental Kelly cells expressing firefly-luciferase were expanded under standard culture conditions and resuspended in PBS before injection of 1×10^6 cells in 200 µl through the tail vein of ten mice. Tumor growth was monitored by BLI as above. Mice were randomized based on BLI and treatment was initiated 7 days after tumor engraftment. Treatment consisted of 350 mg kg^{-1} EPZ-6438 (Seleckchem) administered twice daily by oral gavage for 28 days ($n = 5$ per treatment group). Experimental endpoint was determined as above. One mouse tumor was not processed in the control group due to death from disease prior to harvest.

MG63.3 osteosarcoma in vivo model.

MG63.3 cells were expanded under standard culture conditions as describe above. A total of 1×10^6 cells were resuspended in 100 µl PBS and injected in the right hind leg of ten NSG mice. Seven days after cell engraftment, mice were randomized and the treated group received 350 mg kg^{-1} EPZ-6438 (Seleckchem) administered twice a day by oral gavage for 30 days. Tumors were measured with digital calipers two times a week, and mice were euthanized when tumors reached 15 mm in any dimension. One mouse was excluded from the vehicle group due to a death unrelated to treatment.

CAR T cell production.

The retroviral vector encoding for a GD2-4-1BBz-mCherry CAR was previously described[52]. Briefly, 293GP cells were transiently transfected with plasmids coding for the RD114 envelope proteins and the CAR construct on poly-d-lysine-coated plates using Lipofectamine 2000 (Life Technologies, Invitrogen). Retroviral supernatant was collected 48 and 72 h after transfection and used to transduce human T cells, after activation with anti-CD3/CD28 Dynabeads (Thermo Fisher Scientific) in the presence of interleukin-2 on Retronectin (Takara)-coated plates. Flow cytometry was used to assess transduction efficiency of CAR using the mCherry marker. Mice were treated with 10 million CAR^+ T cells 10 days after activation.

Tumor processing, staining and analysis.

Upon reaching endpoint criteria, mice were euthanized in a CO2 chamber followed by cervical dislocation as a secondary euthanasia method except for those whose brains were harvested as described above for immunohistochemistry.

Tumors were processed for flow cytometry using mechanical-only (SK-N-AS and Kelly flank) or mechanical and chemical (MG63.3 and Kelly metastatic) digestion. For mechanical digestion only, tumors (livers from SK-N-AS mice and flank tumors from Kelly mice) were processed whole on a gentleMACS (Miltenyi Biotec). For mechanical and chemical digestion, tumors (livers from Kelly metastatic mice and hind leg tumors from MG63.3 mice) were chopped into small pieces using sterile razor blades and then incubated with 10 mg ml^{-1} collagenase IV (Worthington Biochemical Corporation) for 3 h, chopping repeatedly every hour. In all cases, cell suspensions were treated twice with ACK lysing buffer (Quality Biological) for 10 min on ice for erythrocyte depletion. Then, samples were passed through a 100-µm cell strainer followed by a 70-µm cell strainer.

For detection of GD2 from tumors in vivo, dinutuximab was used as primary antibody and Alexa Fluor 647-conjugated AffinityPure Donkey anti-human IgG, Fcy fragment (Jackson ImmunoResearch) was used as secondary. This approach ensured that any dinutuximab retained in the tumor was also assessed by flow cytometry. eFluor 780 eBioscience Fixable viability dye (Invitrogen) was used for live/dead discrimination. Tumor cells were identified by excluding anti-mCD45.1 (Invitrogen) cells and then gating on tumor cells as GFP^+, $CD56^+$ (BioLegend) cells for Kelly or GFP^+, $B7\text{-}H3^+$ (R&D) for SK-N-AS and MG63.3.

Statistics and reproducibility.

Representative western blots (Figs. 2a, 4e and 6g and Extended Data Figs. 1e and 3c) are representative of at least two independent experiments. Representative flow cytometry panels (Figs. 1a,d 2c, 3h, 4f, 6a and 8g and Extended Data Figs. 2a,d, 3e, 4b,e, 6a,c,d,f,g, 9a,c and 10c,f) are representative of at least two independent experiments. Micrographs (Fig. 8c and Extended Data Figs. 3d and 10d,e) are representative of at least three independent samples. No statistical methods were used to predetermine sample sizes, but our sample sizes are similar to those reported in previous publications[11]. Data distribution was assumed to be normal, but this was not formally tested. Data collection and analysis were not performed blind to the conditions of the experiments. One mouse was excluded from animal studies reported in Extended Data Fig. 9b,d due to deaths unrelated to treatment and tissue could not be obtained. No other data values were excluded. All in vivo studies were randomized into treatment groups after obtaining sufficient tumor volume or BLI measurements. All experiments for which biological replicates were performed are shown as mean ± s.d. For gene expression assays, data are presented with technical replicates, and are shown as mean ± standard error of the mean. Gene expression assays were performed in at least two independent experiments. For statistical comparisons within two groups, we used a two-tailed Student's *t*-test. For comparisons among multiple groups, we used one-way ANOVA with Tukey's post-hoc test. An adjusted P value of ≤ 0.05 was considered statistically significant for all experiments.

Materials availability.

Further information and requests for reagents should be directed and fulfilled by the lead contacts R.G.M. and K.S.

Reporting summary.

Further information on research design is available in the Nature Research Reporting Summary linked to this article.

Data availability

Complete RNA-, ChIP- and ATAC-sequencing data are available online through the Gene Expression Omnibus (GEO) portal under project accession number GSE180516. The human neuroblastoma data were derived from the TARGET and Treehouse datasets downloaded from the Tumor Compendium v11 Public PolyA (April 2020) on UCSC Treehouse genomics website (available at https://treehousegenomics.soe.ucsc.edu/public-data). Additional human neuroblastoma data were derived from tumor sequencing data available from R2 (https://hgserver1.amc.nl/cgi-bin/r2/main.cgi). Source data files for Figs. 1, 2, 3, 4, 5, 6, 7 and 8 and Extended Data Figs. 1, 2, 3, 4, 6, 7, 9 and 10 have been provided as Source Data Files. All other data supporting the findings of this study are available from the corresponding authors upon reasonable request. Source data are provided with this paper.

Extended Data

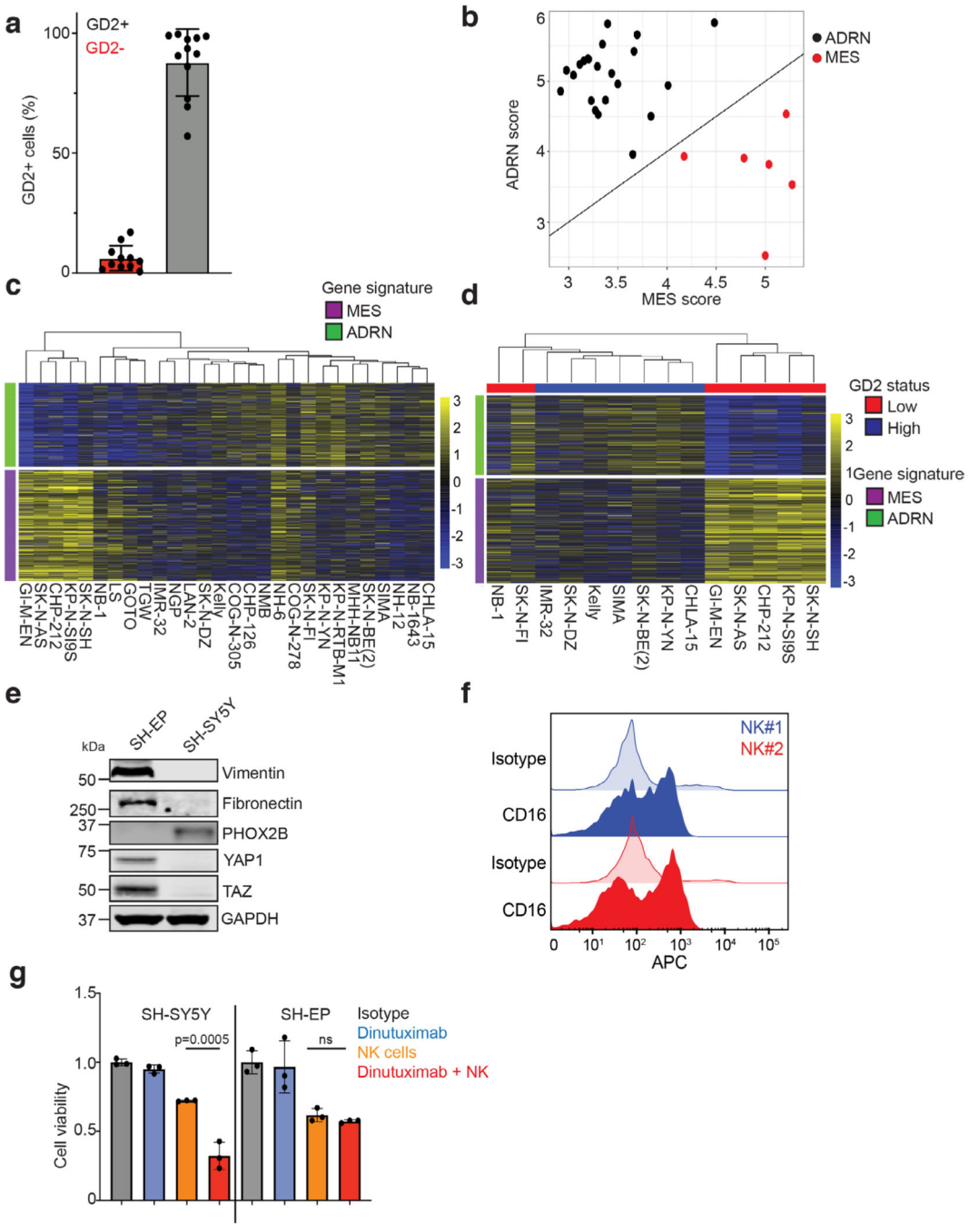

Extended Data Fig. 1 |. Low GD2 expression is correlated with developmental lineage in neuroblastoma cell culture models.

a, Bar plot showing the percentage of GD2 + cells for each cell line from Fig. 1a (n = 12 GD2-high, n = 11 GD2-low). Data are shown as mean ± s.d. **b**, Scatterplot comparing adrenergic (ADRN) and mesenchymal (MES) composite scores for neuroblastoma cell lines in the CCLE. ADRN and MES scores were calculated based on average log2(TPM + 1) expression of all genes within each gene set. Mesenchymal cell lines were called

based on MES score ≥ 4.1 and ADRN score ≤ 5. **c**, Heatmap showing median-center, *Zz*-score normalized RNA sequencing for adrenergic (ADRN, green) and mesenchymal (MES, purple) genes in all neuroblastoma cell lines with RNA-sequencing data available in the CCLE. **d**, Semi-supervised, hierarchical heatmap showing *Zz*-score normalized expression data for mesenchymal (purple) and adrenergic (green) gene sets in cell lines analyzed by differential gene expression analysis and for which GD2 status is shown in Fig. 1a. **e**, Western blot showing expression of mesenchymal markers Vimentin, fibronectin, TAZ and YAP1 and adrenergic marker PHOX2B in SH-EP and SH-SY5Y cell lines. GAPDH is shown as a control. Note that the GAPDH panel is the same bands are shown in Fig. 4a. **f**, Flow cytometry panels demonstrating CD16 staining in two healthy, donor-derived NK cell cultures. **g**, Cell viability for SH-SY5Y or SH-EP cell lines co-cultured with NK cells at an E:T ratio of 1:2 for 48 h and in the presence or absence of 1 μg/mL dinutuximab (n = 3 samples per treatment group). Data are shown mean ± s.d. Significance determined by one-way ANOVA and Tukey's post-hoc test. ns = not significant. Representative data from western blots were confirmed in two independent experiments.

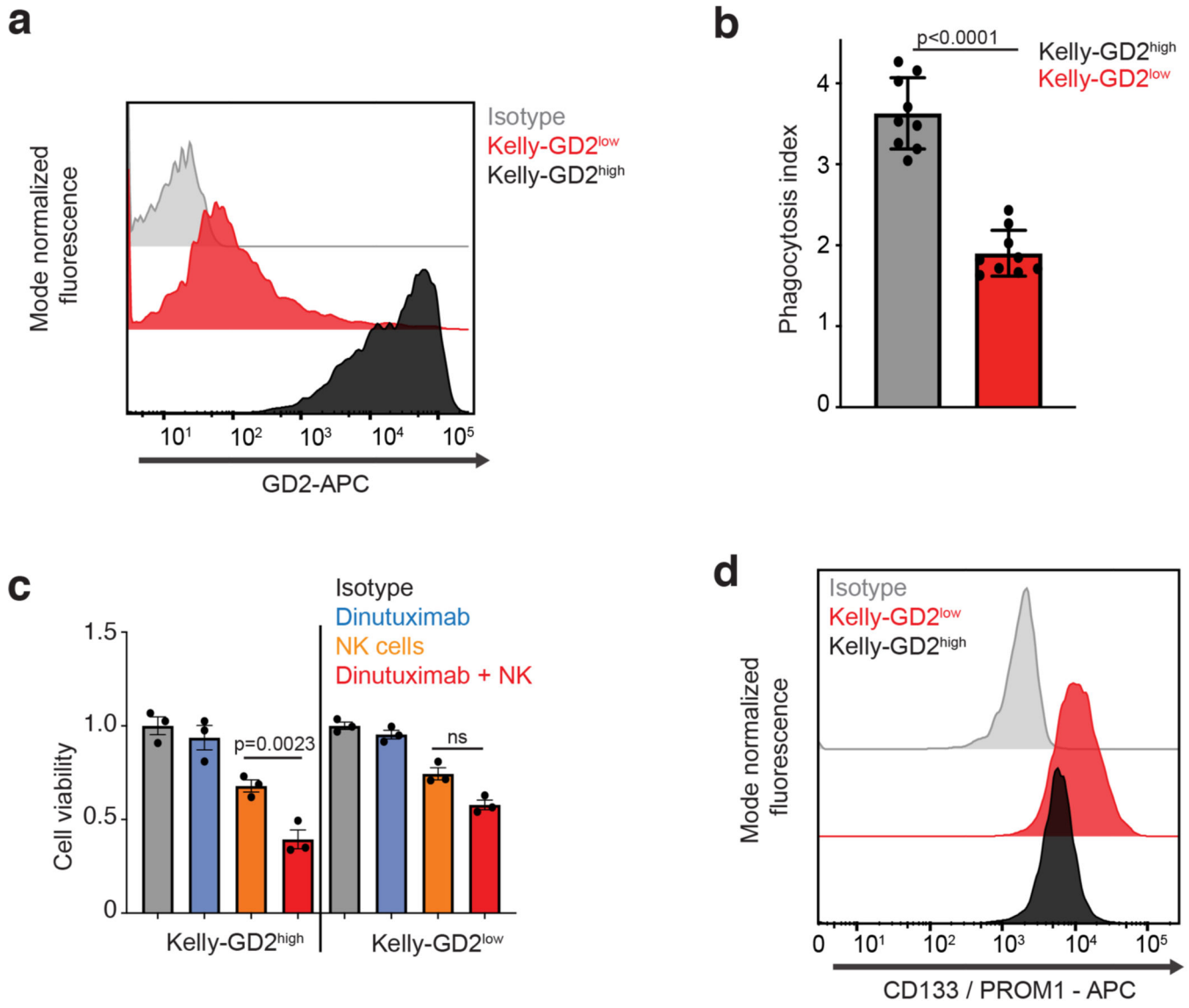

Extended Data Fig. 2 |. GD2 density influences response to anti-GD2 antibody.

a, Parental Kelly cells were sorted based on GD2 expression into Kelly-GD2^{low} (red) or Kelly-GD2^{high} (black) isogenic cell lines. **b**, Kelly-GD2^{low} or Kelly-GD2^{high} were co-cultured with blood-derived macrophages from three healthy donors and measured for phagocytosis in presence or absence of anti-GD2. Data shown is phagocytosis with dinutuximab and normalized to the control condition for that cell line. Triplicates for all three donor cultures were combined. Data are shown mean ± s.d. Significance was determined by two-tailed Mann-Whitney *U* test. **c**, Cell viability for Kelly-GD2^{low} or Kelly-GD2^{high} cell lines co-cultured with NK cells at an E:T ratio of 1:2 for 48 h in the presence or absence of 1 μg/mL dinutuximab (n = 3 samples per treatment group). Data are shown mean ± s.d. Significance determined by one-way ANOVA and Tukey's post-hoc test. **d**, Flow cytometry for Kelly-GD2^{low} and Kelly-GD2^{high} cells for mesenchymal cell marker CD133 (PROM1). ns = not significant. Representative data from flow cytometry were confirmed in two independent experiments.

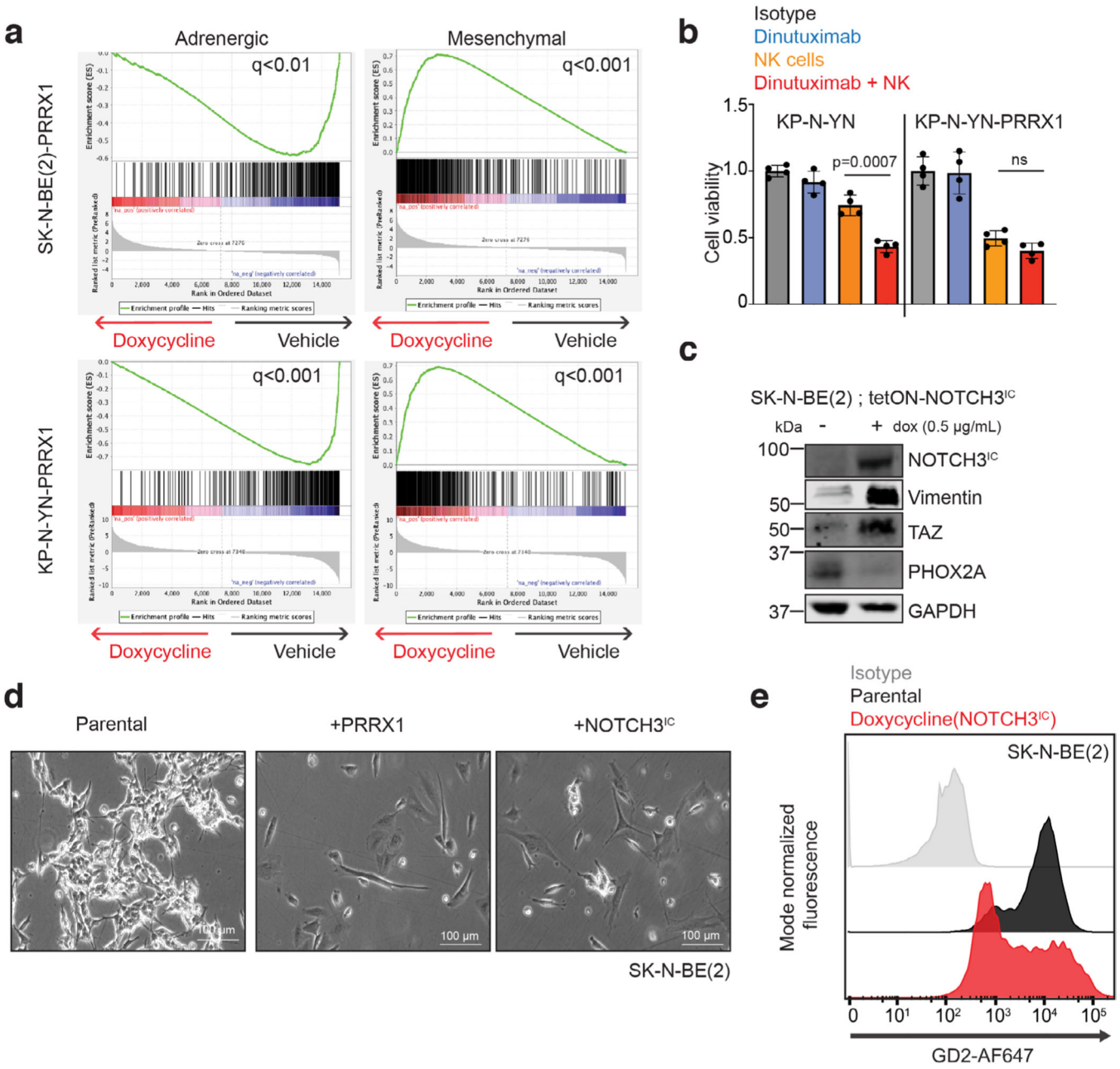

Extended Data Fig. 3 |. Induced Adrenergic-to-Mesenchymal Transition is associated with GD2 downregulation.

a, Gene Set Enrichment Analysis was performed with the neuroblastoma-specific adrenergic or mesenchymal gene signatures for RNA sequencing from vehicle or doxycycline-treated SK-N-BE(2)-tetON-PRRX1 and KP-N-YN-tetON-PRRX1 cell lines. *q*-values are shown. **b**, Cell viability for KP-N-YN induced AMT models co-cultured with NK cells at an E:T ratio of 1:2 in the presence or absence of 1 µg/mL dinutuximab for 8 h ($n = 4$ samples per treatment group). Data are shown as mean ± s.d. Significance determined by one-way ANOVA and Tukey's post-hoc test. **c**, Western blot showing mesenchymal (Vimentin, TAZ, NOTCH3^{IC}) or adrenergic (PHOX2A) markers in parental or NOTCH3^{IC}-expressing

SK-N-BE(2) cells. GAPDH is included as a control. **d**, Representative micrographs (20X) of parental, PRRX1-, or NOTCH3^{IC}-expressing SK-N-BE(2) cells. **e**, Flow cytometry analysis of GD2 for NOTCH3^{IC}-overexpressing SK-N-BE(2) cells. ns = not significant. Representative data from flow cytometry and western blots were confirmed in two independent experiments.

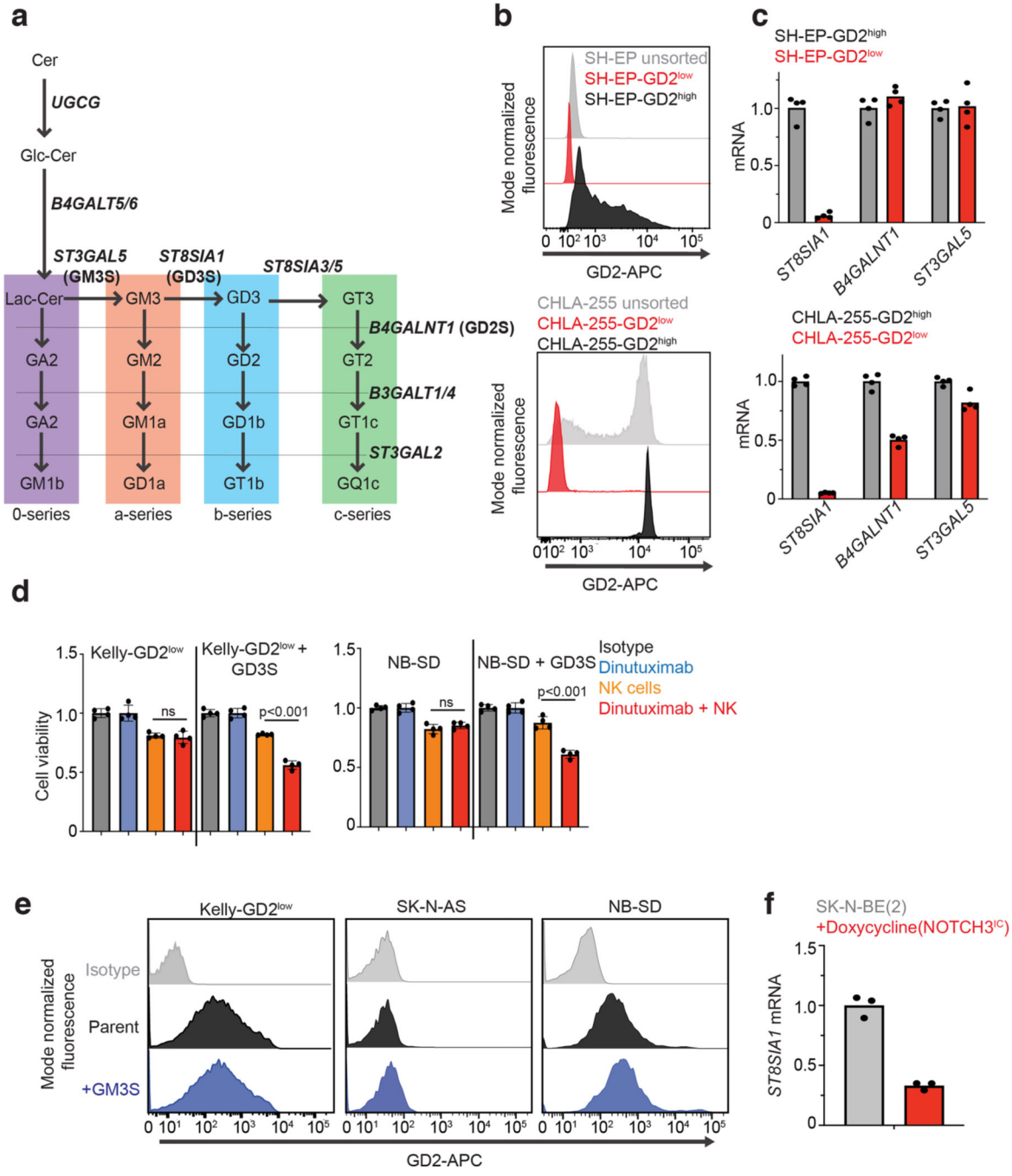

Extended Data Fig. 4 |. Low *ST8SIA1* expression correlates with low surface GD2 and mesenchymal features.

a, Schematic showing the complete ganglioside synthesis pathway. Enzymes responsible for conversion of each ganglioside are labeled in bold and branch points are colored. **b**, Parental SH-EP (top) or CHLA-255 (bottom) cell lines were sorted based on GD2 expression into GD2^{low} (red) or GD2^{high} (black) isogenic cell lines, respectively. **c**, qPCR analysis comparing expression for *ST8SIA1*, *B4GALNT1* and *ST3GAL5* in the SH-EP-GD2^{high} and SH-EP-GD2^{low} (top) or CHLA-255-GD2^{high} and CHLA-255-GD2^{low} (bottom) isogenic cell line pairs. Data derived from a single experiment with 4 technical replicates, experiment was completed once. **d**, Cell viability for Kelly-GD2^{low} and NB-SD with or without GD3 synthase overexpression and co-cultured with NK cells at an E:T ratio of 1:2 and in the presence of absence of 1 μg/mL dinutuximab for 8 h (n = 4 samples per treatment group). Data are shown as mean ± s.d. Significance determined by one-way ANOVA and Tukey's post-hoc test. **e**, Flow cytometry plot showing GD2 expression in Kelly-GD2^{low}, SK-N-AS and NB-SD cell lines with or without constitutive expression of *ST3GAL5*. **f**, qPCR analysis measuring *ST8SIA1* expression in parental or SK-N-BE(2)-NOTCH3^{IC} cells. Data derived from a single experiment with 4 technical replicates, experiment was repeated twice. ns = not significant. Representative data from flow cytometry were confirmed in two independent experiments.

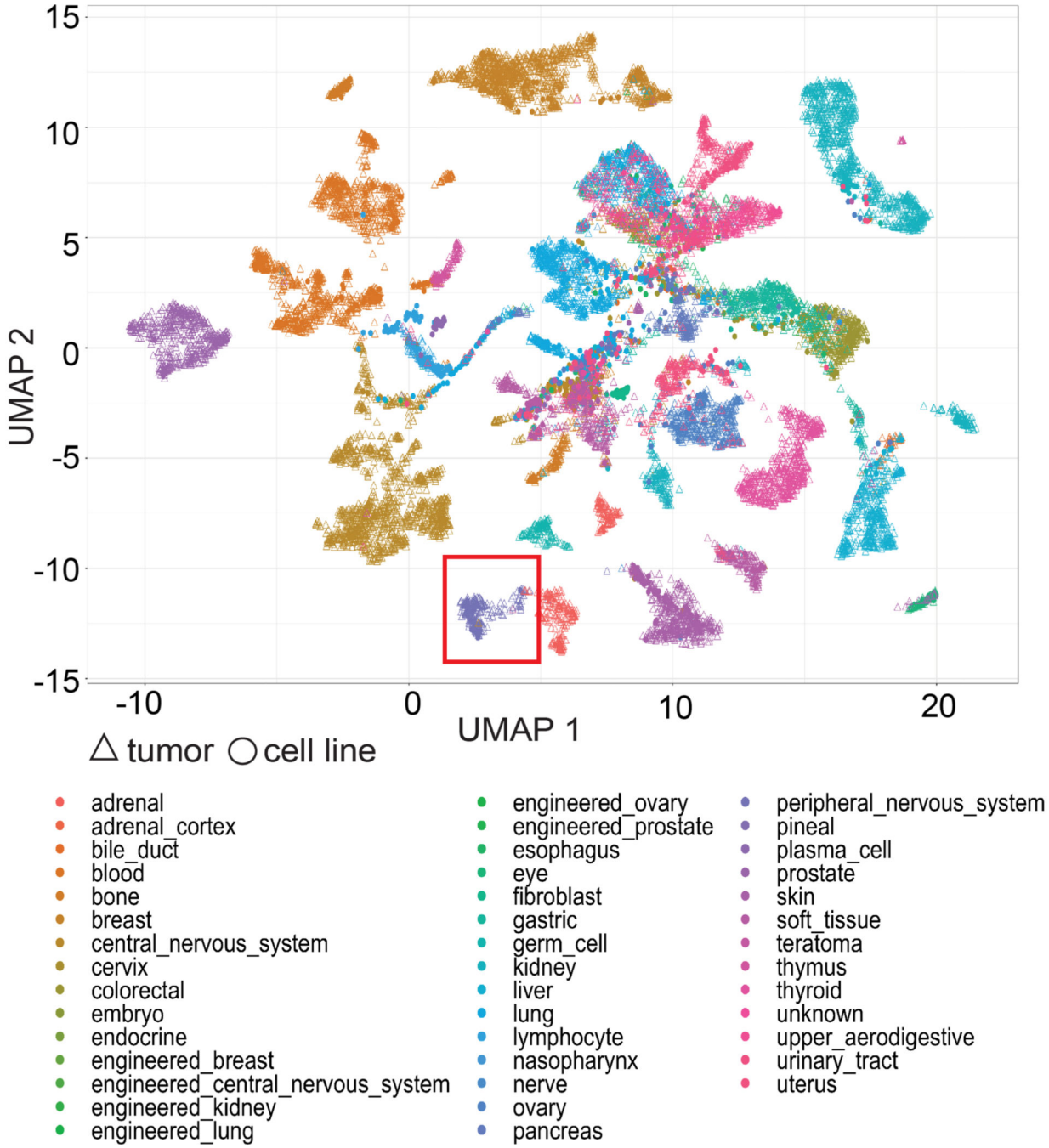

Extended Data Fig. 5 |. Neuroblastoma tumors with mesenchymal properties express reduced GD3 synthase.

UMAP 2D projection plot showing integrated global gene expression for tumors (Treehouse/TARGET) and cell lines (CCLE) from 43 tumor lineages from Celligner. The neuroblastoma lineage is highlighted within the red box.

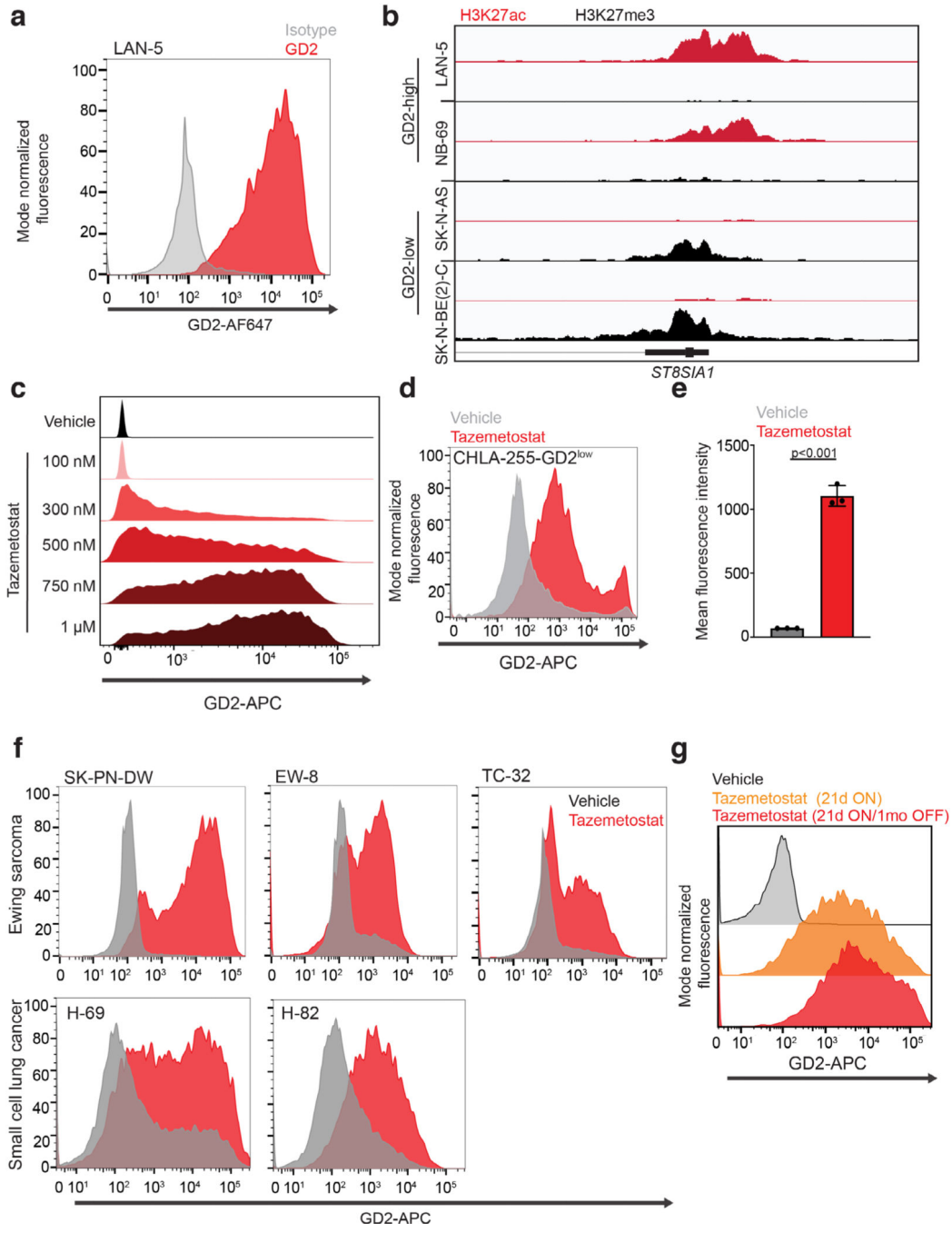

Extended Data Fig. 6 |. EZH2 inhibition restores GD2 expression by reversal of epigenetic silencing of GD3 synthase.

a, Flow Cytometry analysis measuring GD2 expression in LAN-5 cells. **b**, ChIP-seq tracks showing active histone mark H3K27ac and the repressive histone mark H3K27me3 at the *ST8SIA1* locus in LAN-5 (GD2-high), NB-69 (GD2-high), SK-N-AS (GD2-low) and SK-N-BE(2)C (GD2-low) cells from GSE138314. **c**, Flow cytometry panel for GD2 expression in SK-N-AS cells treated with increasing concentrations of tazemetostat. **d**, Flow cytometry plot showing GD2 expression for CHLA255-GD2^{low} cells treated for 21 days with 1 μM

tazemetostat. **e**, Mean fluorescence intensity for GD2 in the flow cytometry data shown in panel **d** (n = 3 samples). Data are shown mean ± s.d. Significance was determined by two-tailed Student's t-test. **f**, Flow cytometry panels showing GD2 expression in Ewing sarcoma cell lines SK-PN-DW, EW-8 and TC-32 treated for 21 days with 1 μM tazemetostat or the small cell lung cancer cell lines H-69 and H-82 cell lines treated for 14 days with 1 μM tazemetostat. **g**, Flow cytometry for GD2 expression in SK-N-AS cells treated for 21 days with 1 μM tazemetostat or treated for 21 days and given a 1-month drug holiday. Representative data from flow cytometry and western blots were confirmed in two independent experiments.

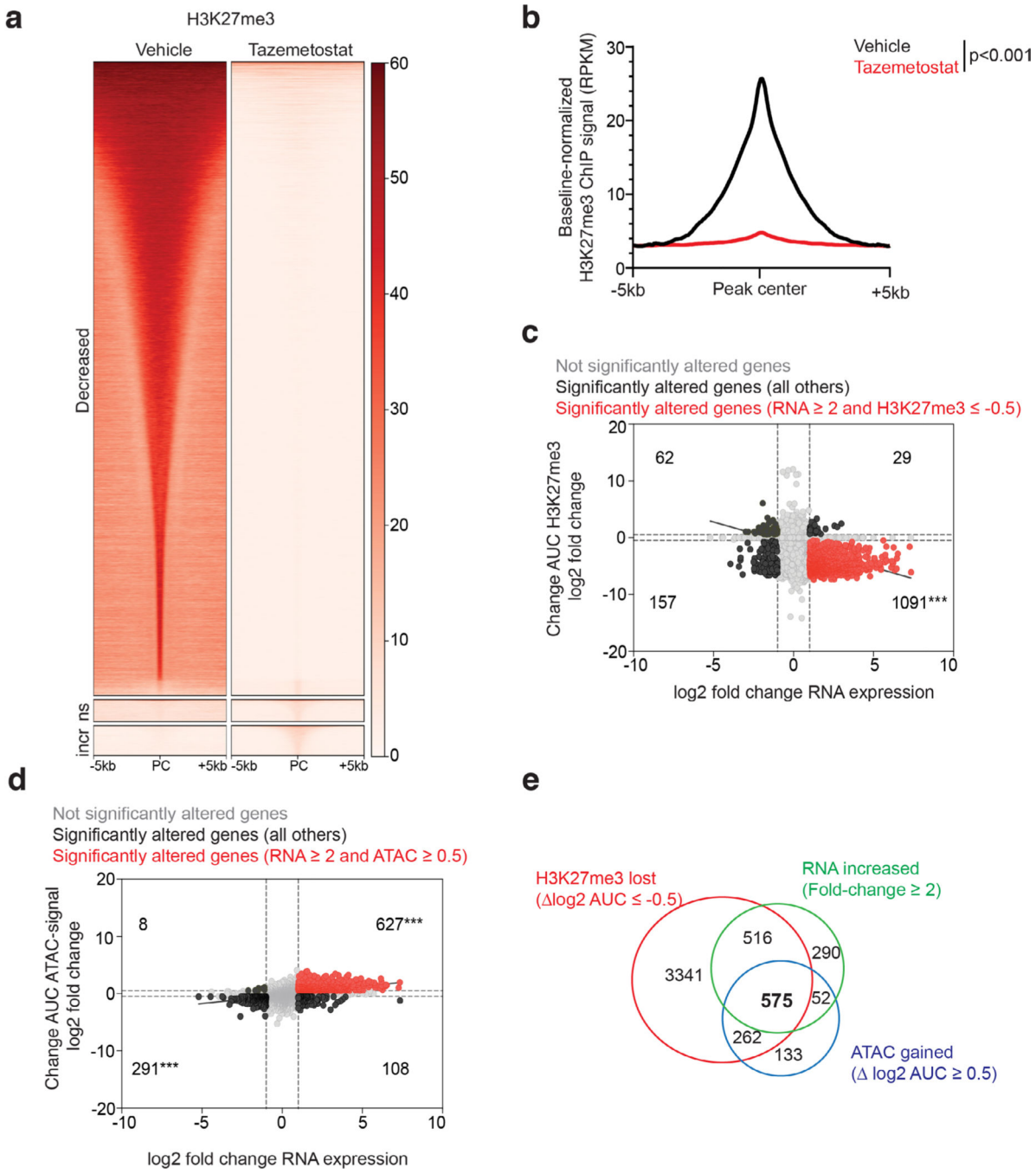

Extended Data Fig. 7 |. Integrated analysis of RNA-, ChIP- and ATAC-sequencing following EZH2 inhibition in SK-N-AS cells.

a, Heatmap showing H3K27me3 ChIP-seq signal at all detected H3K27me3 peaks (88,858). Heatmap is separated into genomic regions with H3K27me3 that are decreased (82,122), unchanged (2,862) or increased (3,874) with 21-day treatment with 1 μM tazemetostat in SK-N-AS cells. PC = peak center, ns = not changed, incr = increased. **b**, Signal enrichment profile plot showing average H3K27me3 enrichment signal for vehicle or tazemetostat treatment groups. Average signal is calculated from 88,858 H3K27me3 peaks. Average

signal was normalized to background signal. Values are shown ±5 kb from the peak center. Significance was determined by two-tailed Student's *t*-test for the area-under-the-curve. **c**, Scatterplot correlating the log2 fold change in H3K27me3 area-under-the-curve (AUC) signal with the log2 fold change in RNA expression. The number of significant genes (fold change of RNA ≥ 2 and H3K27me3 Δ log2 AUC ≤ −0.5) in each quadrant are indicated. Significance for the number of genes within a quadrant was determined by two-tailed Fisher's exact test. **d**, Scatterplot correlating the log2 fold change in ATAC area-under-the-curve (AUC) with the log2 fold change in RNA expression. The number of significant genes (fold change of RNA ≥ 2 and H3K27me3 Δ log2 AUC ≥ 0.5) in each quadrant are indicated. Significance for the number of genes within a quadrant was determined by two-tailed Fisher's exact test. **e**, Venn diagram showing the number of overlapping genes for which H3K27me3 signal was lost, ATAC-seq signal was gained, and RNA expression increased. ***$P < 0.001$.

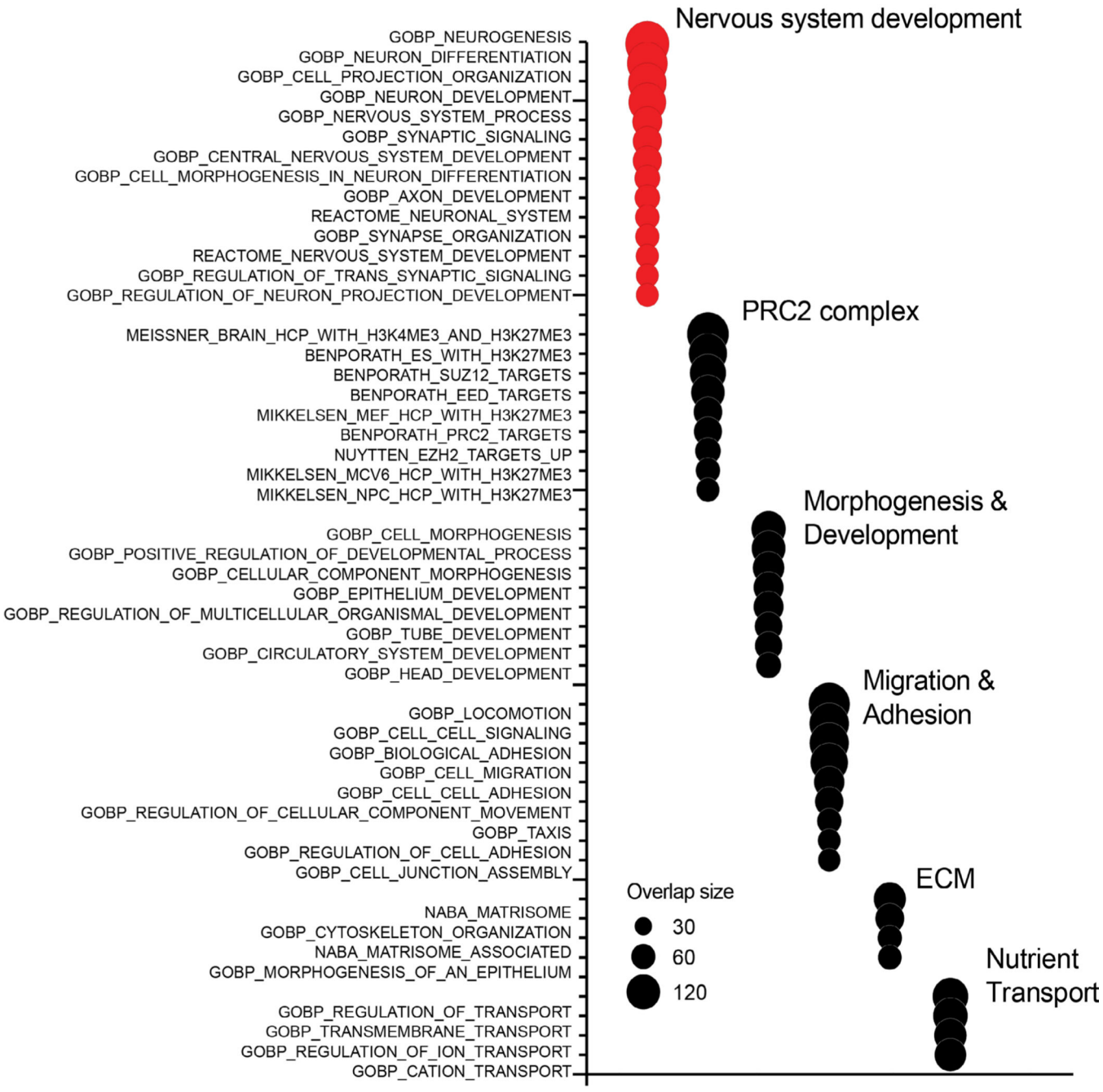

Extended Data Fig. 8 |. Pathways enriched in epigenetically regulated genes from integrated RNA-, ChIP- and ATAC-sequencing following EZH2 inhibition.

Dot plot showing the significant overlap of the 575 genes of interest shown in Extended Data Fig. 7e with C2 and C5 MSigDB libraries. Categories were clustered into the top six most similar pathways. Nervous system development/differentiation-related pathways are indicated in red. Dot size indicates the extent of gene overlap with the indicated gene sets. All gene sets have an FDR of ≤ 0.05 and were calculated by one-tailed Fisher's exact test based on the hypergeometric distribution of the overlapping 575 genes.

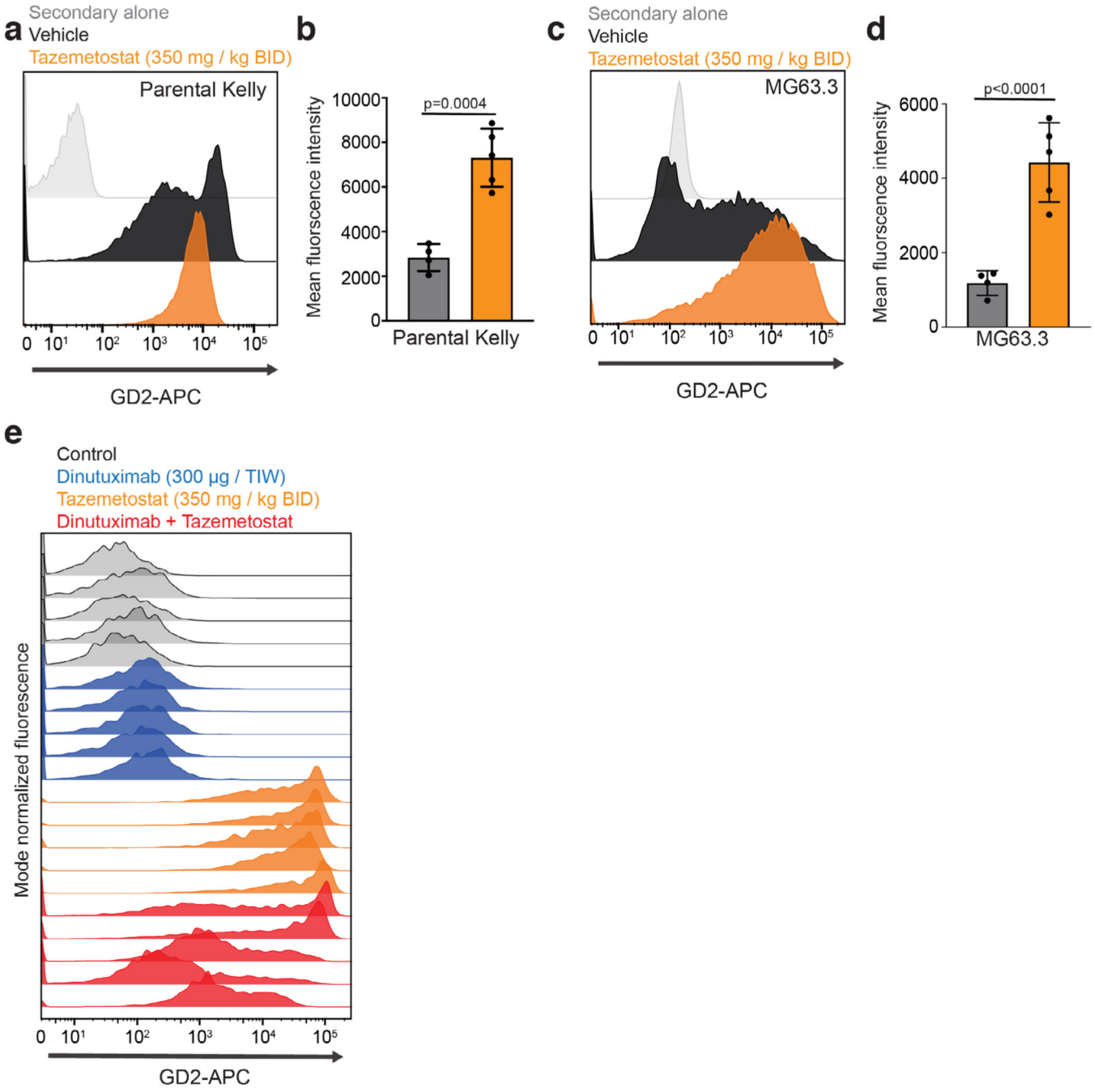

Extended Data Fig. 9 |. EZH2 inhibition increases GD2 density and response to anti-GD2 in multiple models in vivo.

a, Kelly parental cells were injected into the tail vein of NSG mice ($n = 4$ vehicle, $n = 5$ tazemetostat) and treated with 350 mg/kg tazemetostat twice daily or control. Flow cytometry panel showing GD2 expression in representative tumors measured at tumor endpoint. **b**, Quantification of mean fluorescence intensity for GD2 expression for all parental Kelly tumors treated with control ($n = 4$) or tazemetostat ($n = 5$). Data are shown as mean ± s.d. Significance was determined by two-tailed Student's *t*-test. **c**, Representative flow cytometry panel for GD2 from MG63.3 osteosarcoma cells orthotopically injected

into the hind leg of NSG mice (n = 4 vehicle, n = 5 tazemetostat) and treated with 350 mg/kg tazemetostat twice daily. **d**, Quantification of mean fluorescence intensity for GD2 expression in all MG63.3 tumors treated with or without tazemetostat. Data are shown as mean ± s.d. Significance was determined by two-tailed Student's t-test. **e**, Flow cytometry panel for SK-N-AS cells injected into the tail vein of NSG mice (n = 5 per treatment group) and treated with 300 μg dinutuximab three times a week or 500 mg/kg tazemetostat twice daily alone or in combination. Note that one representative tumor from untreated and tazemetostat only groups were shown in Fig. 7A. Representative data from flow cytometry are shown for the biological replicates presented in panels **a** and **c**.

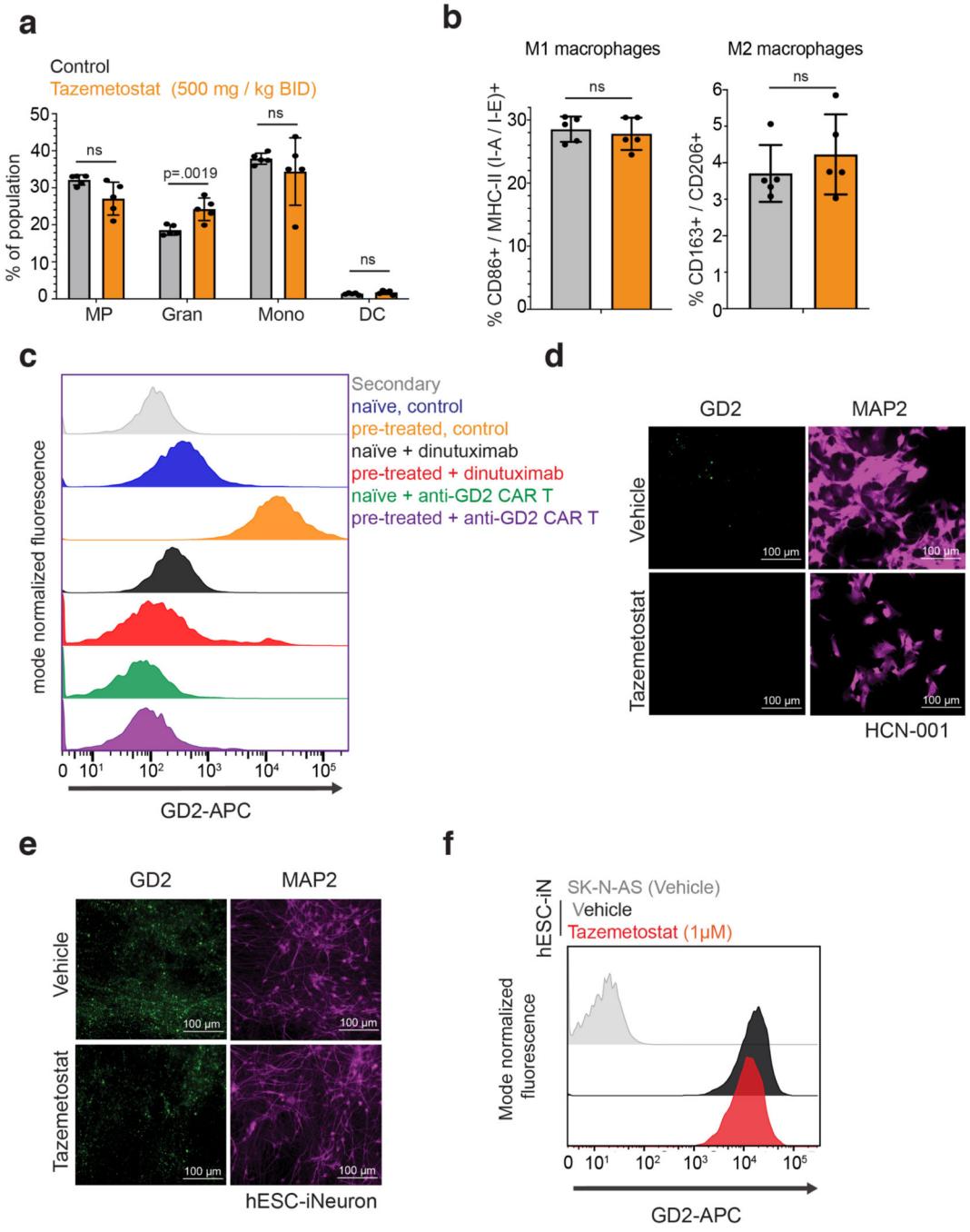

Extended Data Fig. 10 |. EZH2 inhibition increases anti-GD2 response in vivo.

a, Bar plots showing the population of macrophage (MP), granulocyte (Gran), monocyte (Mono) and dendritic cell (DC) populations in each treatment arm (n = 5 per arm) as determined by flow cytometry. Population percentages were determined by the following markers within CD45 + cells: macrophages: CD11b + / F4/80 + ; granulocytes: CD11b + / Ly6G + ; monocytes: CD11b + / Ly6C + ; dendritic cells: CD11c + / MHC-II + . Data are shown as mean ± s.d. Significance was determined by one-way ANOVA and Tukey's post-hoc test. **b**, Bar plots showing the percent of M1 macrophages (CD86 + / MHC-II

(I-A/I-E) +) or M2 macrophages (CD163 + /CD206 +) as a total of the macrophage population (CD11b + / F480 +) (n = 5 per arm). Data are shown as mean ± s.d. Significance was determined by two-tailed Student's t-test. **c**, Flow cytometry showing representative GD2 expression in treatment naïve or tazemetostat pretreated tumors treated with either dinutuximab or anti-GD2 CAR T cells in vivo. **d**,**e**, Immunofluorescence staining for GD2 or neuronal marker MAP2 on vehicle or tazemetostat-treated, passaged primary human cortical cells (**d**) or inducible embryonic stem cells (**e**). **f**, Human embryonic stem cells were differentiated into induced neurons and treated for 14 days with 1 μM tazemetostat. GD2 was measured by flow cytometry. ns = not significant. Representative data from flow cytometry were confirmed in two independent experiments.

Supplementary Material

Refer to Web version on PubMed Central for supplementary material.

Acknowledgements

This research was supported by the National Institutes of Health (NIH; P01 CA217959 to K.S. and R.G.M., R35 CA210030 to K.S., R01-CA227942 to C.R.B. and F30 CA232541 to B.A.H.S), the National Institute of Neurological Disorders and Stroke (R01 NS088355 to K.S., UM1 HG012076 to A.T.S. and R01-NS092597 to M.M), an NIH Director's Pioneer Award (DP1NS111132 to M.M.), the Robert J. Kleberg, Jr. and Helen C. Kleberg Foundation (M.M.), Cancer Research UK (M.M), the Waxman Family Research Fund (M.M. and A.C.G.), the Howard Hughes Medical Institute (M.M.), a Stand Up 2 Cancer (SU2C) Phillip A. Sharp Innovation in Collaboration Award (K.S., M.S. and C.S.M.) and a SU2C Convergence 2.0 grant (M.S. and C.S.M.), Alex's Lemonade Stand (R.G.M.) and the V Foundation (R.G.M.). N.W.M. was supported by the National Cancer Institute under a Ruth L. Kirschstein National Research Service Award (F32 CA261035) and the DFCI Ungerer Fellowship award. R.G.M. is the Taube Distinguished Scholar for Pediatric Immunotherapy at Stanford University School of Medicine. A.T.S. was supported by a Technology Impact Award from the Cancer Research Institute, a Career Award for Medical Scientists from the Burroughs Wellcome Fund and a Pew-Stewart Scholars Award. M.M.M. was supported by the Deutsche Forschungsgemeinshaft (MA 8492/1-1). D.A.S was supported by the Internationales Forschungsstipendium from the Medical Curriculum Munich and the Biomedical Education Program. We thank members of the Program Project Grant and New Approaches to Neuroblastoma Therapy group for their thoughtful comments and suggestions. We thank M. Kararoudi and D. Lee at Nationwide Children's Hospital for their advice and helpfulness with establishing NK cell culture methods.

K.S. consults for and has stock options in Auron Therapeutics, received grant funding from Novartis, served as an advisor for KronosBio and consulted for AstraZeneca and Bristol Meyers Squibb on topics unrelated to this manuscript. R.G.M. is a co-founder of and holds equity in Syncopation Life Sciences and Link Cell Therapies and is a consultant for Lyell Immunopharma, Innvervate Radiopharmaceuticals, NKarta, Immunai, Arovella Therapeutics, Zai lab and Aptorum Group. A.T.S. is a co-founder of Immunai and Cartography Biosciences and receives research funding from Arsenal Biosciences, Merck Research Laboratories and Allogene Therapeutics. C.R.B. is a co-founder of Redwood Biosciences (a subsidiary of Catalent), Enable Biosciences, Palleon Pharmaceuticals, InterVenn Bio, Lycia Therapeutics, OliLux Biosciences, Grace Science and Virsti Therapeutics.

References

1. Smith MA, Altekruse SF, Adamson PC, Reaman GH & Seibel NL Declining childhood and adolescent cancer mortality. Cancer 120, 2497–2506 (2014). [PubMed: 24853691]
2. Park JR et al. Effect of tandem autologous stem cell transplant vs single transplant on event-free survival in patients with high-risk neuroblastoma: a randomized clinical trial. JAMA 322, 746–755 (2019). [PubMed: 31454045]
3. Yu AL et al. Anti-GD2 antibody with GM-CSF, interleukin-2, and isotretinoin for neuroblastoma. N. Engl. J. Med 363, 1324–1334 (2010). [PubMed: 20879881]

4. Yu AL et al. Long-term follow-up of a phase III study of ch14.18 (dinutuximab) + cytokine immunotherapy in children with high-risk neuroblastoma: COG study ANBL0032.Clin. Cancer Res 27, 2179–2189 (2021). [PubMed: 33504555]
5. Cheung NK et al. Murine anti-GD2 monoclonal antibody 3F8 combined with granulocyte-macrophage colony-stimulating factor and 13-cis-retinoic acid in high-risk patients with stage 4 neuroblastoma in first remission. J. Clin. Oncol 30, 3264–3270 (2012). [PubMed: 22869886]
6. Soldatov R. et al. Spatiotemporal structure of cell fate decisions in murine neural crest.Science 364, eaas9536 (2019).
7. Boeva V. et al. Heterogeneity of neuroblastoma cell identity defined by transcriptional circuitries. Nat. Genet 49, 1408–1413 (2017). [PubMed: 28740262]
8. van Groningen T. et al. Neuroblastoma is composed of two super-enhancer-associated differentiation states. Nat. Genet 49, 1261–1266 (2017). [PubMed: 28650485]
9. Gartlgruber M. et al. Super enhancers define regulatory subtypes and cell identity in neuroblastoma. Nat. Cancer 2, 114–128 (2020). [PubMed: 35121888]
10. Berois N. & Osinaga E. Glycobiology of neuroblastoma: impact on tumor behavior, prognosis, and therapeutic strategies. Front. Oncol 4, 114 (2014). [PubMed: 24904828]
11. Theruvath J. et al. Anti-GD2 synergizes with CD47 blockade to mediate tumor eradication. Nat. Med 28, 333–344 (2022). [PubMed: 35027753]
12. Yoshida H. et al. B4GALNT1 induces angiogenesis, anchorage independence growth and motility, and promotes tumorigenesis in melanoma by induction of ganglioside GM2/GD2. Sci. Rep 10, 1199 (2020). [PubMed: 31988291]
13. Wu ZL, Schwartz E, Seeger R. & Ladisch S. Expression of GD2 ganglioside by untreated primary human neuroblastomas. Cancer Res 46, 440–443 (1986). [PubMed: 3940209]
14. Schumacher-Kuckelkorn R. et al. Lack of immunocytological GD2 expression on neuroblastoma cells in bone marrow at diagnosis, during treatment, and at recurrence. Pediatr. Blood Cancer 64, 46–56 (2017). [PubMed: 27654028]
15. Terzic T. et al. Expression of disialoganglioside (GD2) in neuroblastic tumors: a prognostic value for patients treated with anti-GD2 immunotherapy. Pediatr. Dev. Pathol 21, 355–362 (2018). [PubMed: 29067879]
16. Dondero A. et al. Multiparametric flow cytometry highlights B7-H3 as a novel diagnostic/therapeutic target in GD2neg/low neuroblastoma variants. J. Immunother. Cancer 9, e002293 (2021).
17. Davis TA, Czerwinski DK & Levy R. Therapy of B-cell lymphoma with anti-CD20 antibodies can result in the loss of CD20 antigen expression. Clin. Cancer Res 5, 611–615 (1999). [PubMed: 10100713]
18. Fry TJ et al. CD22-targeted CAR T cells induce remission in B-ALL that is naive or resistant to CD19-targeted CAR immunotherapy. Nat. Med 24, 20–28 (2018). [PubMed: 29155426]
19. Majzner RG & Mackall CL Tumor antigen escape from CAR T-cell therapy. Cancer Discov. 8, 1219–1226 (2018). [PubMed: 30135176]
20. Branco FP et al. Loss of HER2 and disease prognosis after neoadjuvant treatment of $HER2^{+}$ breast cancer. Am. J. Transl. Res 11, 6110–6116 (2019). [PubMed: 31632579]
21. Maude SL et al. Tisagenlecleucel in children and young adults with B-cell lymphoblastic leukemia. N. Engl. J. Med 378, 439–448 (2018). [PubMed: 29385370]
22. Mejstrikova E. et al. CD19-negative relapse of pediatric B-cell precursor acute lymphoblastic leukemia following blinatumomab treatment. Blood Cancer J. 7, 659 (2017). [PubMed: 29259173]
23. Keyel ME & Reynolds CP Spotlight on dinutuximab in the treatment of high-risk neuroblastoma: development and place in therapy. Biologics 13, 1–12 (2019). [PubMed: 30613134]
24. Hirabayashi K. et al. Dual-targeting CAR-T cells with optimal co-stimulation and metabolic fitness enhance antitumor activity and prevent escape in solid tumors. Nat. Cancer 2, 904–918 (2021). [PubMed: 34746799]
25. Ross RA, Spengler BA & Biedler JL Coordinate morphological and biochemical interconversion of human neuroblastoma cells. J. Natl Cancer Inst 71, 741–747 (1983). [PubMed: 6137586]

26. Takenobu H. et al. CD133 suppresses neuroblastoma cell differentiation via signal pathway modification. Oncogene 30, 97–105 (2011). [PubMed: 20818439]
27. van Groningen T. et al. A NOTCH feed-forward loop drives reprogramming from adrenergic to mesenchymal state in neuroblastoma. Nat. Commun 10, 1530 (2019). [PubMed: 30948783]
28. Ruckhaberle E. et al. Gene expression of ceramide kinase, galactosyl ceramide synthase and ganglioside GD3 synthase is associated with prognosis in breast cancer. J. Cancer Res. Clin. Oncol 135, 1005–1013 (2009). [PubMed: 19125296]
29. Warren A. et al. Global computational alignment of tumor and cell line transcriptional profiles. Nat. Commun 12, 22 (2021). [PubMed: 33397959]
30. Upton K. et al. Epigenomic profiling of neuroblastoma cell lines. Sci. Data 7, 116 (2020). [PubMed: 32286315]
31. Margueron R. & Reinberg D. The Polycomb complex PRC2 and its mark in life. Nature 469, 343–349 (2011). [PubMed: 21248841]
32. Hu N, Strobl-Mazzulla PH & Bronner ME Epigenetic regulation in neural crest development. Dev. Biol 396, 159–168 (2014). [PubMed: 25446277]
33. Kailayangiri S. et al. EZH2 inhibition in Ewing sarcoma upregulates GD2 expression for targeting with gene-modified T cells. Mol. Ther 27, 933–946 (2019). [PubMed: 30879952]
34. Wang C. et al. EZH2 mediates epigenetic silencing of neuroblastoma suppressor genes CASZ1, CLU, RUNX3, and NGFR. Cancer Res. 72, 315–324 (2012). [PubMed: 22068036]
35. Qadeer ZA et al. ATRX in-frame fusion neuroblastoma is sensitive to EZH2 inhibition via modulation of neuronal gene signatures. Cancer Cell 36, 512–527 e519 (2019). [PubMed: 31631027]
36. Chen L. et al. CRISPR-Cas9 screen reveals a MYCN-amplified neuroblastoma dependency on EZH2. J. Clin. Invest 128, 446–462 (2018). [PubMed: 29202477]
37. Reppel L. et al. Targeting disialoganglioside GD2 with chimeric antigen receptor-redirected T cells in lung cancer.J. Immunother. Cancer 10, e003897 (2022).
38. Shusterman S. et al. Antitumor activity of hu14.18-IL2 in patients with relapsed/refractory neuroblastoma: a Children's Oncology Group (COG) phase II study. J. Clin. Oncol 28, 4969–4975 (2010). [PubMed: 20921469]
39. Yin J. et al. Ezh2 regulates differentiation and function of natural killer cells through histone methyltransferase activity. Proc. Natl. Acad. Sci. U S A 112, 15988–15993 (2015). [PubMed: 26668377]
40. Yin Y. et al. EZH2 suppression in glioblastoma shifts microglia toward M1 phenotype in tumor microenvironment. J. Neuroinflammation 14, 220 (2017). [PubMed: 29132376]
41. Zhang X. et al. Macrophage/microglial Ezh2 facilitates autoimmune inflammation through inhibition of Socs3. J. Exp. Med 215, 1365–1382 (2018). [PubMed: 29626115]
42. Schramm A. et al. Mutational dynamics between primary and relapse neuroblastomas. Nat Genet 47, 872–877 (2015). [PubMed: 26121086]
43. Iniguez AB et al. Resistance to epigenetic-targeted therapy engenders tumor cell vulnerabilities associated with enhancer remodeling. Cancer Cell 34, 922–938 (2018). [PubMed: 30537514]
44. Ruan S. & Lloyd KO Glycosylation pathways in the biosynthesis of gangliosides in melanoma and neuroblastoma cells: relative glycosyltransferase levels determine ganglioside patterns. Cancer Res. 52, 5725–5731 (1992). [PubMed: 1394196]
45. Lo Piccolo MS, Cheung NK & Cheung IY GD2 synthase: a new molecular marker for detecting neuroblastoma. Cancer 92, 924–931 (2001). [PubMed: 11550167]
46. Cheung IY, Lo Piccolo MS, Collins N, Kushner BH & Cheung NK Quantitation of GD2 synthase mRNA by real-time reverse transcription-polymerase chain reaction: utility in bone marrow purging of neuroblastoma by anti-GD2 antibody 3F8. Cancer 94, 3042–3048 (2002). [PubMed: 12115395]
47. Jansky S. et al. Single-cell transcriptomic analyses provide insights into the developmental origins of neuroblastoma. Nat. Genet 53, 683–693 (2021). [PubMed: 33767450]
48. Dong R. et al. Single-cell characterization of malignant phenotypes and developmental trajectories of adrenal neuroblastoma. Cancer Cell 38, 716–733 (2020). [PubMed: 32946775]

49. Sequist LV et al. Genotypic and histological evolution of lung cancers acquiring resistance to EGFR inhibitors. Sci. Transl. Med 3, 75ra26 (2011).
50. Aggarwal R, Zhang T, Small EJ & Armstrong AJ Neuroendocrine prostate cancer: subtypes, biology, and clinical outcomes. J. Natl Compr. Canc. Netw 12, 719–726 (2014). [PubMed: 24812138]
51. Neo WH et al. MicroRNA miR-124 controls the choice between neuronal and astrocyte differentiation by fine-tuning Ezh2 expression. J. Biol. Chem 289, 20788–20801 (2014). [PubMed: 24878960]
52. Mount CW et al. Potent antitumor efficacy of anti-GD2 CAR T cells in H3-K27M^{+} diffuse midline gliomas. Nat. Med 24, 572–579 (2018). [PubMed: 29662203]
53. Majzner RG et al. GD2-CAR T cell therapy for H3K27M-mutated diffuse midline gliomas. Nature, Epub ahead of print. PMID 35130560. PMCID: PMC8967714 (2022).
54. van den Bijgaart RJE et al. Combined sialic acid and histone deacetylase (HDAC) inhibitor treatment up-regulates the neuroblastoma antigen GD2. J. Biol. Chem 294, 4437–4449 (2019). [PubMed: 30670592]
55. Kroesen M. et al. Anti-GD2 mAb and vorinostat synergize in the treatment of neuroblastoma. Oncoimmunology 5, e1164919 (2016). [PubMed: 27471639]
56. Italiano A. et al. Tazemetostat, an EZH2 inhibitor, in relapsed or refractory B-cell non-Hodgkin lymphoma and advanced solid tumours: a first-in-human, open-label, phase 1 study. Lancet Oncol. 19, 649–659 (2018). [PubMed: 29650362]
57. Gounder M. et al. Tazemetostat in advanced epithelioid sarcoma with loss of INI1/SMARCB1: an international, open-label, phase 2 basket study. Lancet Oncol. 21, 1423–1432 (2020). [PubMed: 33035459]
58. Morschhauser F. et al. Tazemetostat for patients with relapsed or refractory follicular lymphoma: an open-label, single-arm, multicentre, phase 2 trial. Lancet Oncol. 21, 1433–1442 (2020). [PubMed: 33035457]
59. Majzner RG et al. Tuning the antigen density requirement for CAR T-cell activity. Cancer Discov. 10, 702–723 (2020). [PubMed: 32193224]
60. Li H. & Durbin R. Fast and accurate long-read alignment with Burrows-Wheeler transform. Bioinformatics 26, 589–595 (2010). [PubMed: 20080505]
61. Ramirez F. et al. deepTools2: a next generation web server for deep-sequencing data analysis. Nucleic Acids Res. 44, W160–W165 (2016). [PubMed: 27079975]
62. Zhang Y. et al. Model-based analysis of ChIP-seq (MACS). Genome Biol. 9, R137 (2008). [PubMed: 18798982]
63. Pohl A. & Beato M. bwtool: a tool for bigWig files. Bioinformatics 30, 1618–1619 (2014). [PubMed: 24489365]
64. Carroll TS, Liang Z, Salama R, Stark R. & de Santiago I. Impact of artifact removal on ChIP quality metrics in ChIP-seq and ChIP-exo data. Front. Genet 5, 75 (2014). [PubMed: 24782889]
65. Yu G, Wang LG & He QY ChIPseeker: an R/Bioconductor package for ChIP peak annotation, comparison and visualization. Bioinformatics 31, 2382–2383 (2015). [PubMed: 25765347]
66. Corces MR et al. An improved ATAC-seq protocol reduces background and enables interrogation of frozen tissues. Nat. Methods 14, 959–962 (2017). [PubMed: 28846090]
67. Barbie DA et al. Systematic RNA interference reveals that oncogenic KRAS-driven cancers require TBK1. Nature 462, 108–112 (2009). [PubMed: 19847166]
68. Barkal AA et al. CD24 signalling through macrophage Siglec-10 is a target for cancer immunotherapy. Nature 572, 392–396 (2019). [PubMed: 31367043]
69. Zhang Y. et al. Rapid single-step induction of functional neurons from human pluripotent stem cells. Neuron 78, 785–798 (2013). [PubMed: 23764284]
70. Marro SG et al. Neuroligin-4 regulates excitatory synaptic transmission in human neurons. Neuron 103, 617–626 (2019). [PubMed: 31257103]

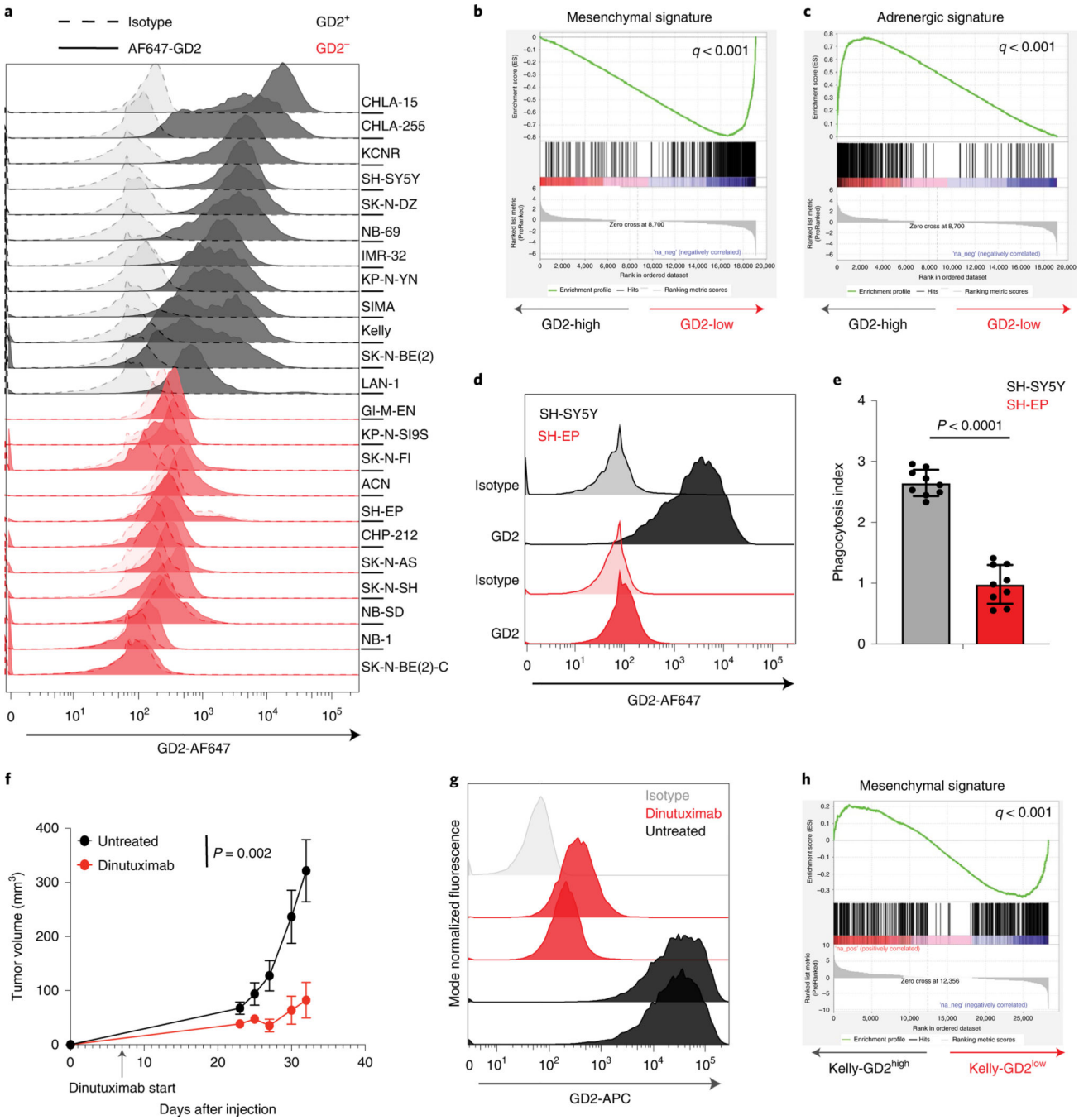

Fig. 1 |. Low GD2 expression is correlated with developmental lineage in neuroblastoma cell line models.

a, Flow cytometry measuring GD2 expression across 23 neuroblastoma cell lines. Cell lines are colored based on the percentage of GD2 cells in the population compared to the secondary antibody (≥50%; black). Dashed lines represent isotype antibody control. **b**,**c**, Differential gene expression analysis was performed between GD2^{+} (n = 7) and GD2^{-} (n = 7) cell lines found in the CCLE database and rank ordered from highest to lowest expression in GD2+ cell lines. GSEA was performed on the neuroblastoma-specific, mesenchymal (**b**)

or adrenergic (**c**) gene signatures. *q*-values are shown. **d**, Flow cytometry analysis showing GD2 staining in adrenergic SH-SY5Y or mesenchymal SH-EP cell lines. **e**, SH-EP or SH-SY5Y were co-cultured with blood-derived macrophages from three healthy donors and measured for phagocytosis in the presence or absence of dinutuximab. Data shown is phagocytosis with anti-GD2 normalized to the control condition for that cell line. Triplicates for three donors were combined ($n = 9$ samples). Data are shown mean ± standard deviation (s.d.). Significance determined by two-tailed Mann-Whitney *U* test. **f**, 2×10^6 parental Kelly cells were injected into the flank of NSG mice, which were either treated with 300 μg dinutuximab ($n = 4$) intraperitoneally or untreated ($n = 4$) three times weekly starting on day 7. Tumors were measured with digital calipers two to three times weekly. Data are shown mean ± s.d. Significance was determined by two-way analysis of variance (ANOVA). **g**, Flow cytometry showing GD2 expression in dinutuximab-treated or untreated Kelly tumors shown in panel **f**. **h**, RNA sequencing was performed for Kelly-GD2^{low} and Kelly-GD2^{high} cell lines, and genes were rank ordered based on differential gene expression analysis. GSEA was run on the neuroblastoma-specific mesenchymal gene set. Representative data from flow cytometry and western blots were confirmed in two independent experiments. APC = allophycocyanin.

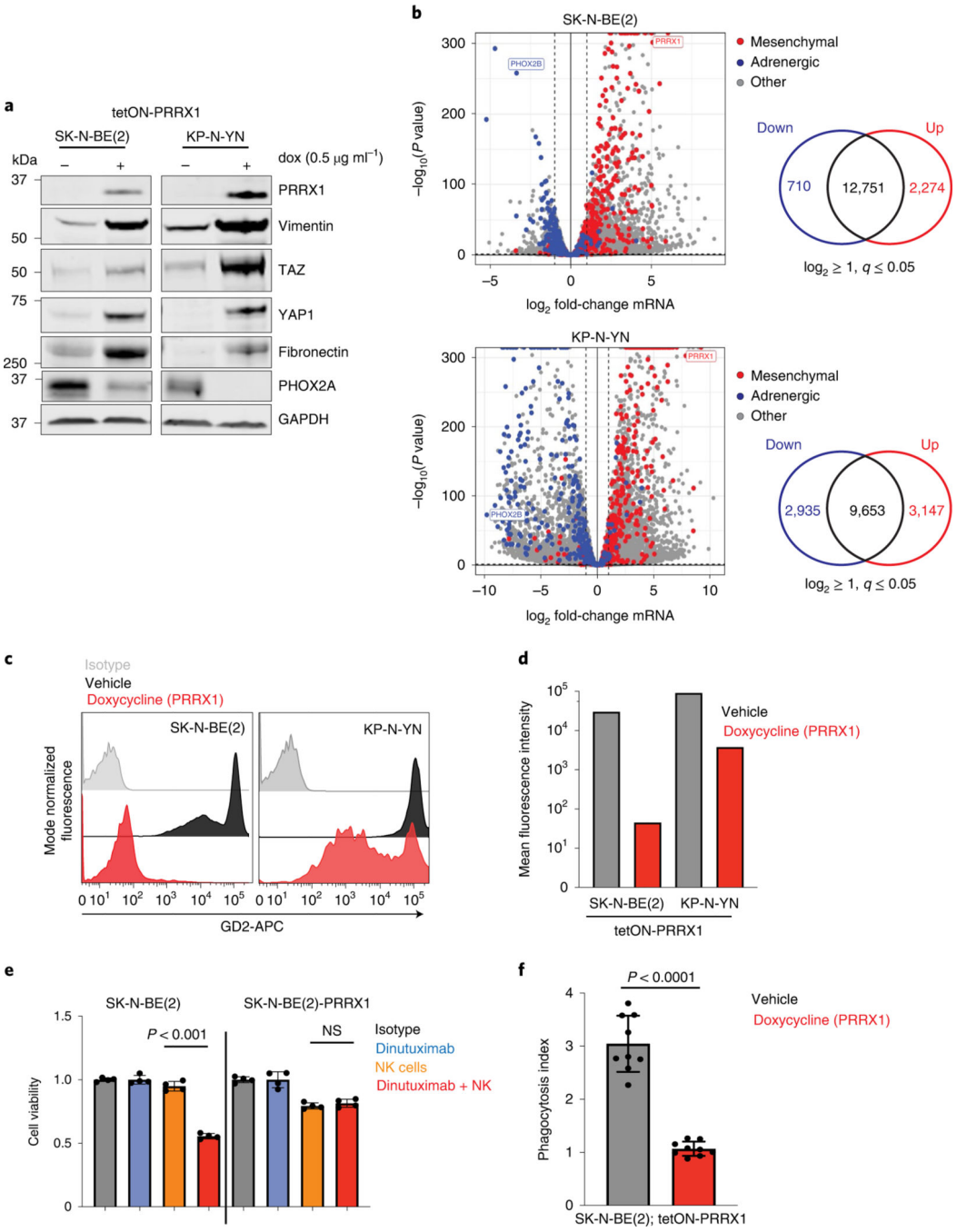

Fig. 2 |. AMT induction represses GD2 expression and response to anti-GD2 antibody.

a, SK-N-BE(2) and KP-N-YN cell lines were infected with a tetON-PRRX1 transcription factor conjugated to HA. Cell lines were cultured for 21 days in the presence of 500 ng ml^{-1} doxycycline (dox), and protein lysates were measured for expression of mesenchymal markers PRRX1, vimentin, TAZ, YAP1, fibronectin and adrenergic marker PHOX2A. GAPDH is a loading control. **b**, Volcano plots showing differential gene expression analysis from RNA sequencing for doxycycline-treated or naive SK-N-BE(2)-PRRX1 and KP-N-YN-PRRX1 cell lines. Genes were colored based on their belonging in adrenergic (blue) or

mesenchymal (red) gene sets. Venn diagrams indicate differential expressed genes (adjusted *P* value < 0.05; $\log_2$ fold change ≥1). *PHOX2B* and *PRRX1* transcripts are indicated on the volcano plots. *P* values were calculated by false discovery rate calculation using DESeq2 on two-sided apeglm settings. **c**, Representative flow cytometry plots showing GD2 expression for SK-N-BE(2)-PRRX1 or KP-N-YN-PRRX1 cell lines treated with doxycycline (red) or control (black) or isotype control (gray). **d**, Mean fluorescence intensity for GD2 staining shown in panel **c**. **e**, Cell viability for the SK-N-BE(2)-induced AMT model co-cultured with NK cells at an effector to target (E/T) ratio of 1:2 and in the presence of absence of 1 μg ml^{-1} dinutuximab for 8 h ($n = 4$ samples per treatment group). Data are shown as mean ± s.d. Significance determined by one-way ANOVA and Tukey's post-hoc test. **f**, SK-N-BE(2)-PRRX1 cell lines were co-cultured in the presence or absence of dinutuximab with blood-derived macrophages from three healthy donors and measured for phagocytosis. Data shown is phagocytosis with dinutuximab normalized to the control condition for that cell line. Triplicates for all three donor cultures were combined. Data are shown mean ± s.d. Significance determined by two-tailed Mann–Whitney *U* test. NS, not significant. Representative data from flow cytometry and western blots were confirmed in three independent experiments.

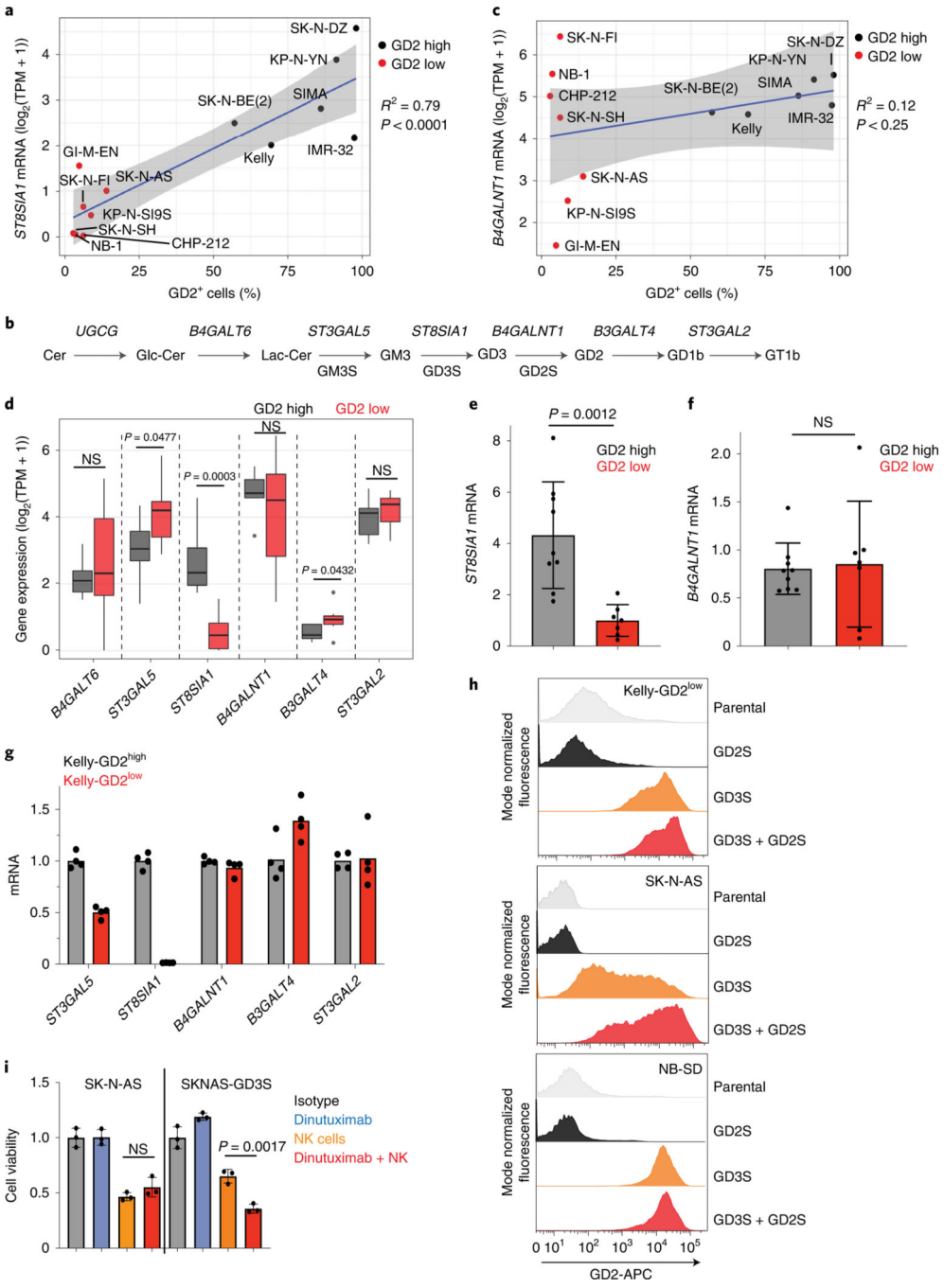

Fig. 3 |. GD2 downregulation is correlated with reduced GD3S expression.

a, Scatterplot showing the correlation of the percentage of GD2$^+$ cells in each cell line against the expression of GD3 synthase (*ST8SIA1*) from the CCLE. Linear regression line is shown, and gray cloud denotes 95% two-tailed confidence interval. R^2 and *P* values are indicated. TPM, transcripts per million. **b**, Schematic showing the b-series ganglioside synthesis pathway. Gene names for enzymes that are responsible for the conversion of each product are labeled in italics, and protein abbreviations are labeled in bold. **c**, Scatterplot showing the correlation of the percentage of GD2+ cells against the expression of GD2

synthase (*B4GALNT1*) from the CCLE. Linear regression line is shown, and gray cloud denotes 95% two-tailed confidence interval. R^2 and *P* values are indicated. **d**, Box-and-whisker plots comparing $\log_2$(TPM + 1) normalized expression for selected ganglioside synthase enzymes in GD2-low ($n = 7$) or GD2-high ($n = 7$) cell lines found in the CCLE data. Boxes show median, 25% quartile and 75% quartile; whiskers denote smallest and largest values within 1.5 times the interquartile range. Dots outside of the whiskers denote significant outliers. Significance was determined by two-tailed Student's *t*-test within each gene. **e**,**f**, qPCR analysis comparing expression of *ST8SIA1* (**e**) or *B4GALNT1* (**f**) in representative GD2-high ($n = 9$ biological replicates) or GD2-low ($n = 7$ biological replicates) cell lines. Significance was determined by two-tailed Student's *t*-test within each gene. Data are shown as mean ± s.d. **g**, qPCR analysis comparing expression for a panel of ganglioside synthase enzymes in Kelly-GD2^{high} and Kelly-GD2^{low} cells. Data derived from a single experiment with four technical replicates, experiment was repeated twice. **h**, Representative flow cytometry plots for GD2 expression in Kelly-GD2^{low}, SK-N-AS or NB-SD cell lines transduced to overexpress GD2 synthase, GD3 synthase or both together. **i**, Cell viability for SK-N-AS cells ±GD3S overexpression that were co-cultured with NK cells at an E/T ratio of 1:2 for 48 h in the presence or absence of 1 μg ml^{-1} dinutuximab ($n = 3$ samples per treatment group). Data are shown mean ± s.d. Significance determined by one-way ANOVA and Tukey's post-hoc test. Representative data from flow cytometry were confirmed in two independent experiments.

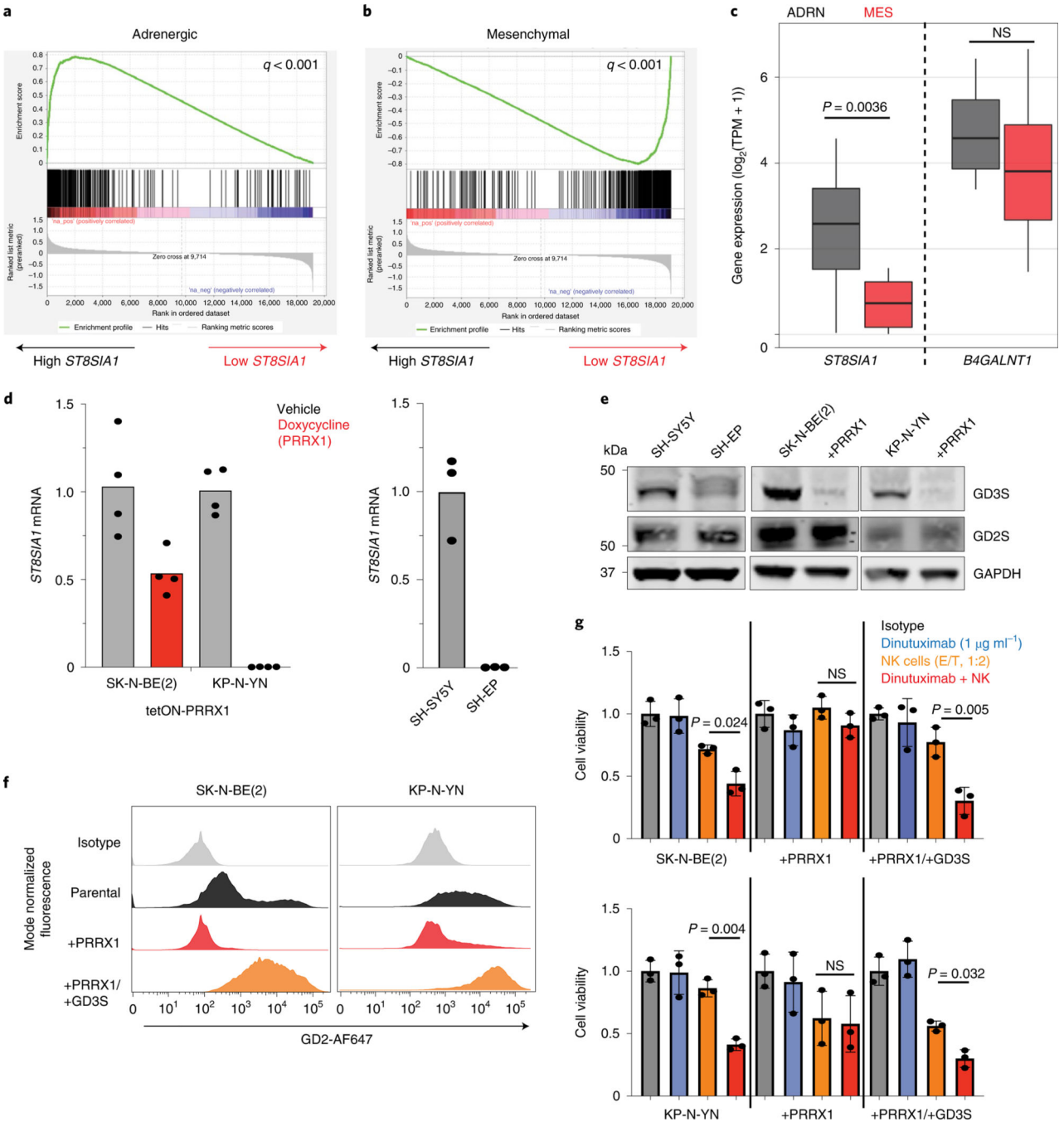

Fig. 4 |. GD3S downregulation is correlated with AMT.

a,**b**, Pearson correlations were generated for *ST8SIA1* against expression for all other genes in neuroblastoma cell lines found in the CCLE ($n = 31$) and rank-ordered based on most to least correlated. GSEA was performed on neuroblastoma-specific, adrenergic (A) or mesenchymal (B) gene sets. q-values are shown. **c**, Box-and-whisker plot comparing $\log_2$(TPM + 1) normalized expression for *ST8SIA1* and *B4GALNT1* in ADRN ($n = 25$) or MES ($n = 6$) cell lines found in the CCLE. Boxes show median, 25% quartile and 75% quartile; whiskers denote smallest and largest values within 1.5 times the interquartile

range. Significance was determined by two-tailed Student's *t*-test for each individual gene. **d**, qPCR analysis for *ST8SIA1* in three models of AMT (SK-N-BE(2)-PRRX1, KP-N-YN-PRRX1 and SH-EP/SH-SY5Y). Data are derived from a single experiment with four (SK-N-BE(2) and KP-N-YN) or three (SH-EP/SH-SY5Y) technical replicates, and the experiment was repeated twice. **e**, Western blot showing protein expression for GD3S and GD2S in three AMT models. GAPDH is included as a loading control. Note that GAPDH for SH-EP and SH-SY-5Y are the same bands as shown in Extended Data Fig. 1e. **f**, Flow cytometry showing GD2 expression in parental, PRRX1-transduced or PRRX1-transduced + GD3S SK-N-BE(2) and KP-N-YN cell lines. **g**, Cell viability for SK-N-BE(2) and KP-N-YN cell lines shown in panel **f**. Cell lines were co-cultured with NK cells at an E/T ratio of 1:2 for 48 h and in the presence or absence of 1 μg ml^{-1} dinutuximab ($n = 3$ samples per treatment group). Data are shown mean ± s.d. Significance determined within each cell line by one-way ANOVA and Tukey's post-hoc test. Representative data from flow cytometry and western blots were confirmed in two independent experiments.

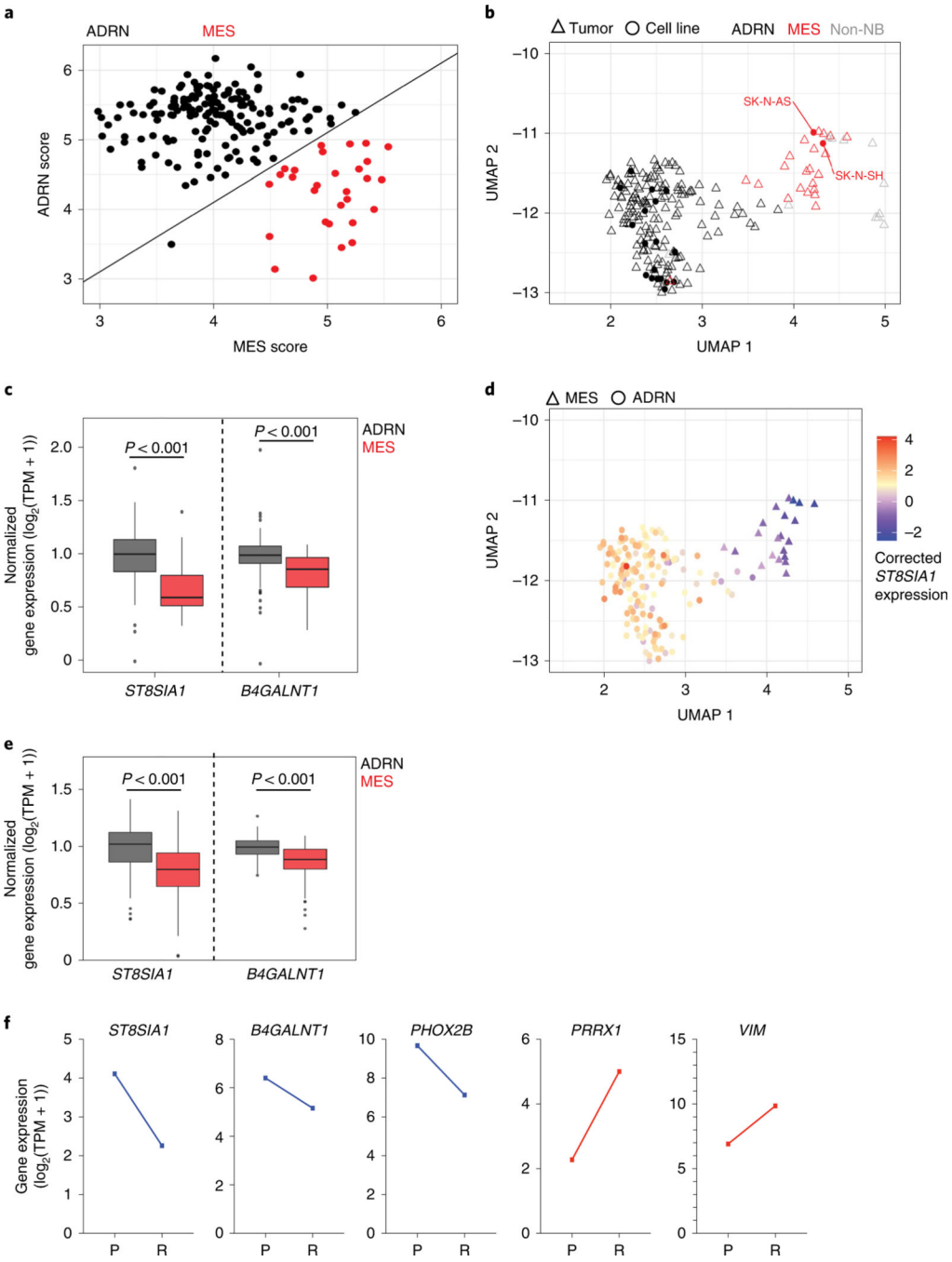

Fig. 5 |. Neuroblastoma tumors with mesenchymal properties express reduced *ST8SIA1*.

a, Adrenergic and mesenchymal composite scores were calculated based on an averaged $\log_2$(TPM + 1) expression of all genes within each gene set. Mesenchymal cell lines were called based on MES score ≥4.5 and ADRN score ≤5. **b**, UMAP 2D projection plot focused on neuroblastoma (NB) showing the clustering of tumor and cell line global expression profiles. Cell lines (circles) and tumors (triangles) were determined to be adrenergic or mesenchymal in panel **a** and labeled in black and red, respectively. **c**, Box-and-whisker plot comparing $\log_2$(TPM + 1) gene expression for *ST8SIA1* and *B4GALNT1* enzymes

in adrenergic (n = 174) or mesenchymal (n = 116) TARGET/Treehouse tumors. Boxes show median, 25% quartile and 75% quartile; whiskers denote smallest and largest values within 1.5 times the interquartile range. Dots outside of the whiskers denote significant outliers. Expression values were normalized to the mean expression in adrenergic tumors. Significance was determined by two-tailed Student's *t*-test within each gene. **d**, Celligner-corrected *ST8SIA1* gene expression from TARGET/Treehouse tumor data overlaid in the Celligner UMAP projections from panel **b**. **e**, RNA sequencing from Gartlgruber et al. (R2) showing box-and-whisker plots comparing $\log_2$(TPM + 1) gene expression for *ST8SIA1* and *B4GALNT1* enzymes in adrenergic (n = 427) or mesenchymal (n = 152) tumors. Boxes show median, 25% quartile and 75% quartile; whiskers denote smallest and largest values within 1.5 times the interquartile range. Dots outside of the whiskers denote significant outliers. Expression values were normalized to the mean expression in adrenergic tumors. Significance was determined by two-tailed Student's *t*-test within each gene. **f**, Log_2(TPM + 1) RNA-sequencing reads for a matched adrenergic primary (P) and mesenchymal relapsed (R) neuroblastoma tumors in Gartlgruber et al.

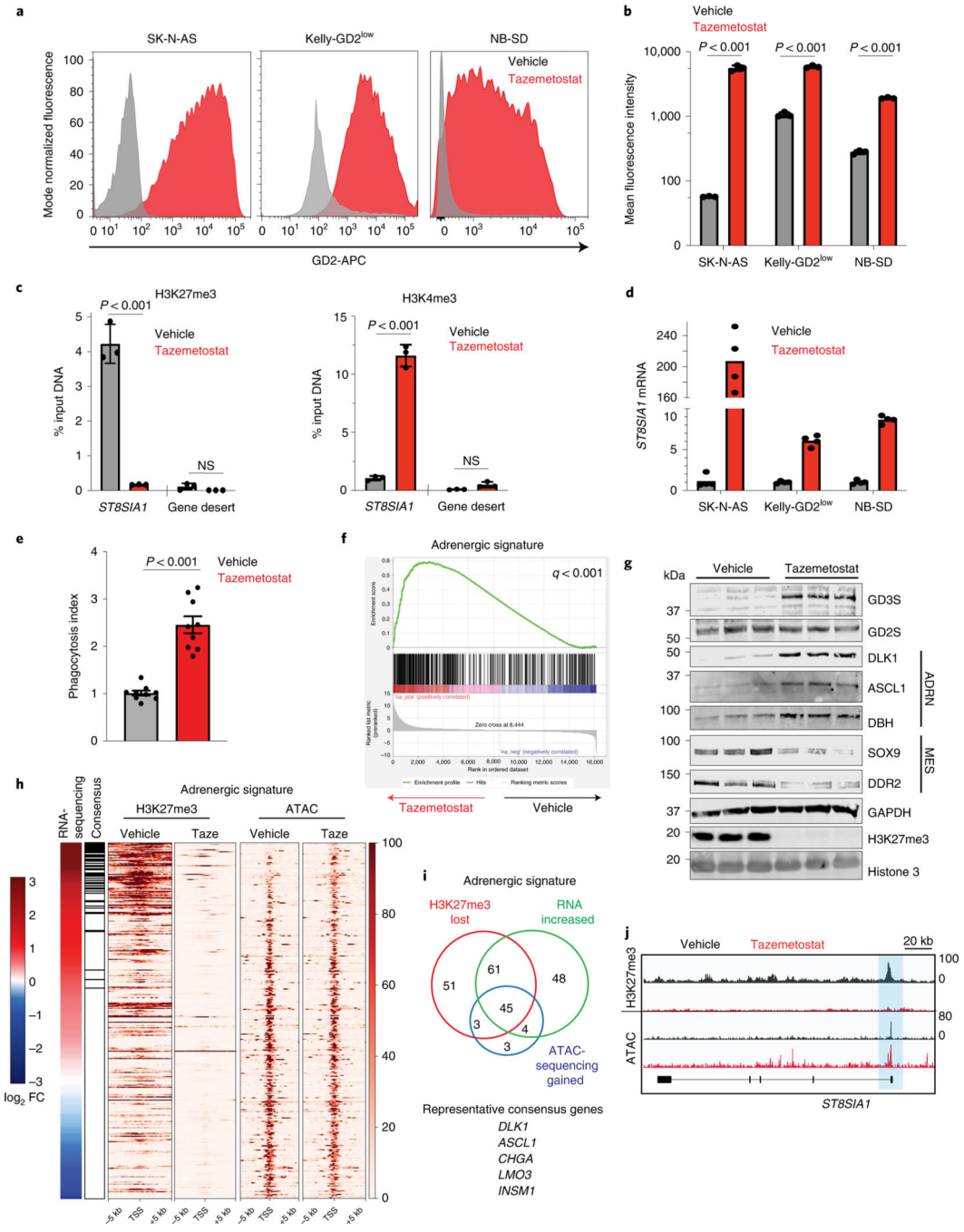

Fig. 6 |. epigenetic inhibition results in transcriptional reprogramming and restoration of GD2 expression.

a, Flow cytometry showing GD2 expression in GD2-low cell lines treated with vehicle or tazemetostat for 21 days. **b**, Mean fluorescence intensity for GD2 in cell lines in panel **a**. Data are shown mean ± s.d. ($n = 3$ samples). Significance was determined by two-tailed Student's *t*-test. **c**, ChIP-qPCR for H3K27me3 and H3K4me3 marks at the *ST8SIA1* promoter and gene desert in SK-N-AS cells treated with tazemetostat. Significance was determined by one-way ANOVA and Tukey's post-hoc test. Data are shown as mean ± s.d.

(*n* = 3 biological replicates). **d**, *ST8SIA1* qPCR expression in vehicle or tazemetostat-treated cell lines. Data derived from a single experiment with four technical replicates, experiment was repeated twice. **e**, SK-N-AS treated with vehicle or tazemetostat were co-cultured with blood-derived macrophages from three healthy donors and measured for phagocytosis in the presence or absence of anti-GD2. Triplicates for all three donor cultures were combined (*n* = 9 per treatment group). Data are shown mean ± s.d. Significance determined by two-tailed Mann-Whitney *U* test. **f**, GSEA for the adrenergic neuroblastoma gene signature from RNA sequencing between SK-N-AS cell lines treated with tazemetostat or vehicle. **g**, Western blot showing expression for ganglioside synthesis enzymes, adrenergic markers and mesenchymal markers in vehicle or tazemetostat-treated SK-N-AS cells. **h**, Heatmap showing RNA expression for the adrenergic gene set and corresponding enrichment for H3K27me3 or ATAC sequencing in vehicle- or tazemetostat (Taze)-treated SK-N-AS cells. Heatmap is ordered by $\log_2$ fold change (FC) from RNA sequencing. Black bars indicate a subset of consensus genes for which there was statistically significant loss of H3K27me3, upregulation of RNA and gain of chromatin accessibility. H3K27me3 and ATAC signal enrichment is shown for genomic regions ±5 kb from the transcriptional start site (TSS). **i**, Venn diagram showing the number of overlapping genes within the adrenergic gene set for which there is significantly reduced H3K27me3, significantly increased RNA expression or significantly more chromatin accessibility. Representative core genes from the 45 at the intersection of all three datasets are shown. **j**, ChIP- and ATAC-sequencing tracks for *ST8SIA1* (GRCh38) in SK-N-AS cells treated with vehicle or tazemetostat. Blue boxes indicate significantly altered peaks. Representative data from flow cytometry were confirmed in three independent experiments and western blots were confirmed in two independent experiments.

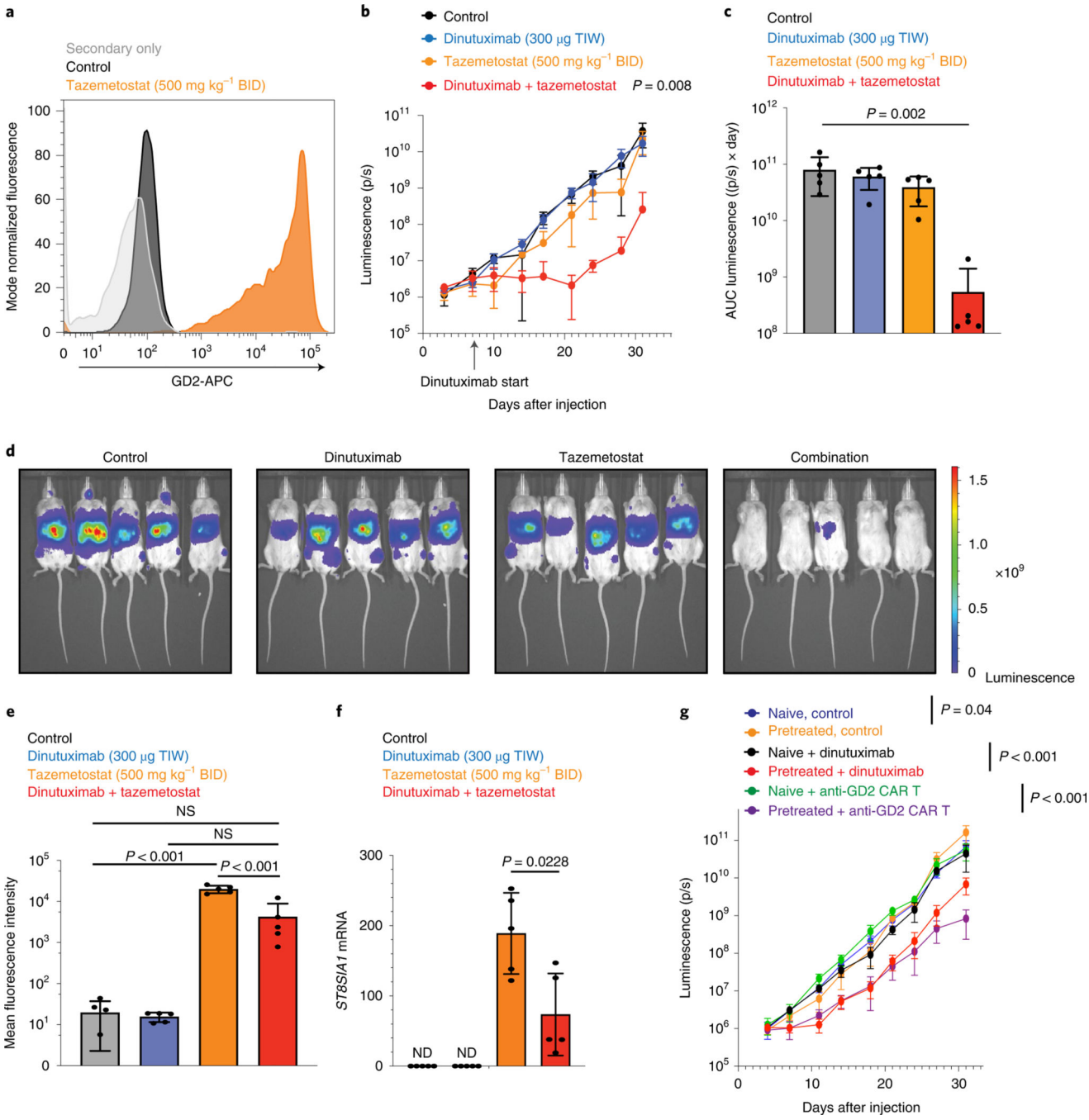

Fig. 7 |. EZH2 inhibition significantly enhances GD2 expression and response to anti-GD2 in vivo.

a, Flow cytometry showing GD2 expression from mice bearing metastatic SK-N-AS tumors treated with 500 mg kg^{-1} tazemetostat twice daily (BID) or control. **b**, Tumor growth curves for SK-N-AS cells injected into the tail vein of NSG mice ($n = 5$ per treatment group) and treated with 300 μg dinutuximab intraperitoneally three times a week (TIW) or 500 mg kg^{-1} tazemetostat orally twice daily alone or in combination. Data are shown mean ± s.d. Significance for combination treatment against other treatment groups was determined

by two-way ANOVA. **c**, Bioluminescence AUC measurements for tumors in each treatment arm ($n = 5$). Data are shown mean ± s.d. Significance determined by one-way ANOVA and Tukey's post-hoc test as compared to control. **d**, Representative bioluminescence imaging for mice in each treatment group as measured on day 28. **e**, Mean fluorescence intensity for GD2 in control, dinutuximab, tazemetostat and dinutuximab + tazemetostat-treated tumors at study endpoint ($n = 5$). Data are shown mean ± s.d. Significance was determined by one-way ANOVA and Tukey's post-hoc test. **f**, qPCR analysis showing *ST8SIA1* expression at endpoint in control, dinutuximab-, tazemetostat- or tazemetostat + dinutuximab-treated tumors ($n = 5$ biological replicates). Data are shown mean ± s.d. and normalized relative to *ST8SIA1* expression in SK-N-AS cells cultured in vitro. ND, not detected. Significance was determined by two-tailed Student's *t*-test between tazemetostat and combination. **g**, Tumor growth curves for SK-N-AS cells that were pretreated for 21 days with 1 μM tazemetostat or vehicle and then injected into the tail vein of NSG mice. Mice were randomized into untreated, treated with 300 μg dinutuximab intraperitoneally three times weekly or treated with anti-GD2 CAR T infusion groups ($n = 5$ per arm), and tumor burden measured via BLI over time. Data are shown mean ± s.d. Significance for the anti-GD2 treatment against control groups was determined by one-way ANOVA. Representative data from flow cytometry were confirmed in two independent experiments.

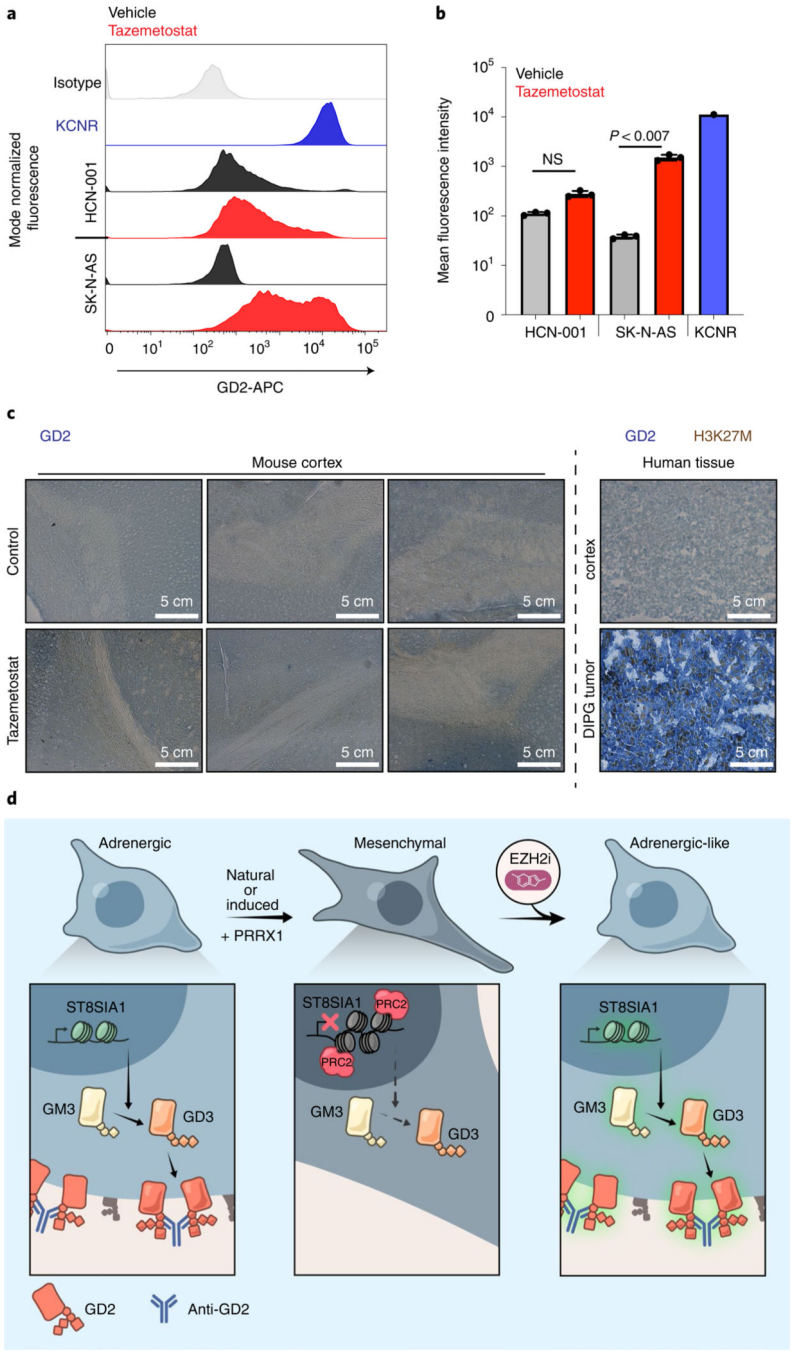

Fig. 8 |. eZH2 inhibition does not significantly upregulate GD2 expression in healthy tissue.

a, Flow cytometry panel showing GD2 expression in low-passage (p + 3), primary cortical neurons (HCN-001) and the mesenchymal neuroblastoma cell line SK-N-AS after treatment with tazemetostat. **b**, Mean fluorescence intensity measurements for groups shown in Fig. 7g ($n = 3$). Data are shown as mean ± s.d. Significance was determined by one-way ANOVA and Tukey's post-hoc test. **c**, Immunohistochemistry showing GD2 staining in the mouse cortex of mice treated for 28 days with 350 mg kg^{-1} tazemetostat ($n = 3$) or control ($n = 3$). Uninvolved human tissue from matched human cortex and GD2-expressing human

diffuse intrinsic pontine glioma (DIPG) tumor sections are included as controls for low and high GD2 expression, respectively. GD2 expression is stained in blue, and H3K27M (human tissue only) is stained in brown. **d**, Schema showing proposed mechanism of GD2 regulation. GD2 is highly expressed on the cell surface of neuroblastoma cells expressing an adrenergic transcriptional program. Transition from an adrenergic state to a mesenchymal state decreases GD2 expression through downregulation of *ST8SIA1*, rendering cells nonresponsive to anti-GD2 immunotherapy. Treatment with an EZH2 inhibitor induces an adrenergic-like state through transcriptional, epigenetic and chromatin remodeling, thereby re-expressing *ST8SIA1*, increasing GD2 expression and restoring sensitivity to anti-GD2 antibody. Representative data from flow cytometry were confirmed in two independent experiments.